12-2011

# ELECTRICAL DETECTION OF MECHANICAL RESONANCE IN NANOTUBES AND SEMICONDUCTING NANOWIRES

Doyl Dickel
*Clemson University*, ddickel@g.clemson.edu

# ELECTRICAL DETECTION OF MECHANICAL RESONANCE IN NANOTUBES AND SEMICONDUCTING NANOWIRES

---

A Dissertation
Presented to
the Graduate School of
Clemson University

---

In Partial Fulfillment
of the Requirements for the Degree
Doctor of Philosophy
Physics

---

by
Doyl Edward Dickel
December 2011

---

Accepted by:
Dr. Apparao M. Rao, Committee Chair
Dr. Malcolm J. Skove
Dr. Murray S. Daw
Dr. Catalina Marinescu

# ABSTRACT

In recent years, there has been substantial interest in the development of microelectro-mechanical systems (MEMS) and even nanoelectro-mechanical systems (NEMS) for use in a wide variety of applications both as experimental tools (refs) and in a continuing effort to decrease the size and cost and increase the efficiency of electrical components. In particular, cantilevered nanometer beams have been a recent focus due to a number of interesting properties, including enhanced field emission, high tensile strength, and piezoelectric properties. The ability to accurately determine the electrical and mechanical properties of these cantilevers is paramount in assessing their feasibility as MEMS and NEMS components, as well as developing technology to utilize them.

In this thesis, a unique method for determining these properties is presented. By developing a fully electrical system for the actuation and detection of a nano-cantilever's mechanical resonance, an important step in furthering the development of NEMS technology has been achieved. The mathematics of this system are developed in-depth, for a pair of synthesized nanostructures, multi-walled nanoubes (MWNTs), and coiled carbon nanotubes (cCNTs), measurements of their material properties are calculated from their resonant behavior and a number of potential applications are explored.

# DEDICATION

For my mother, Kathy Dickel, whose constant love and support have helped guide me every day of my life.

# ACKNOWLEDGMENTS

To everyone who has supported me during my graduate career, I give my most sincere thanks. Special thanks go out to those who have helped develop this dissertation and my studies in general.

Thanks go to my advisor, Dr. Apparao Rao. He has been instrumental in the direction of this project, and in keeping me moving forward, while letting me conduct such interesting research.

Dr. Malcolm Skove has been a constant source of wisdom and guidance. Without his thoughtful, often humorous, input, my research would have ended literally before it began. And without his countless hours spent reading and revising manuscripts, it would never have ended. He has also always been willing to lend an ear or a kind word. I am lucky to have been afforded so much of his time and to count him as a friend.

It would be remiss of me not to also thank the individuals who have worked with HDR over the years or who have helped me as I have progressed. Thanks to Dr. Jay Gaillard for creating the foundation of which I have tried to build and helping me understand it all those years ago, to Dr. Gayatri Keskar who worked extensively to develop applications of HDR and to develop our understand of Duffing behavior in these systems, to Dr. Ramakrishna Podila for countless discussions, a hundred good ideas, and a wonderful friendship, to Dr. Bevan Elliott and Bert Behlow for their work on the content presented in Chapter 3, to Deepika Saini for all the late nights watching dials and screens, and a special thank you to Dr. Murray Daw for his guidance, advice, and wisdom, and for entertaining my crazy idea that I wanted to do theory on the side.

TABLE OF CONTENTS

Page

TITLE PAGE ..... i

ABSTRACT ..... ii

DEDICATION ..... iii

ACKNOWLEDGMENTS ..... iv

LIST OF TABLES ..... viii

LIST OF FIGURES ..... ix

CHAPTER

I. INTRODUCTION ..... 1

1.1 Introduction ..... 1
1.2 Modern Nano-Cantilevers ..... 2
1.3 Nano-Cantilever Excitation ..... 3
1.4 Electrical Actuation and Detection in Nano-Cantilevers ..... 4
1.4.1 Piezoresistive and Piezoelectrical Detection ..... 5
1.4.2 Field Emission Detection ..... 6
1.4.3 Capacitive Detection ..... 7

II. THE HARMONIC DETECTION OF RESONANCE METHOD ..... 9

2.1 The Need for Harmonic Detection of Resonance ..... 9
2.1.1 Electrostatic Driving of Cantilevers ..... 9
2.2 Characterization of HDR ..... 12
2.2.1 Equation of Motion for a Simple Harmonic Oscillator ..... 12
2.2.2 Equation of Motion for HDR ..... 14
2.2.3 Simplifying Approximations ..... 15
2.2.4 Features of Our Solution ..... 21
2.2.5 Limaçon Behavior ..... 24
2.3 Experimental Verification of HDR ..... 25
2.4 Nonlinear Behavior ..... 32

Table of Contents (Continued)

Page

III. ELECTRICAL DETECTION OF RINGDOWN BEHAVIOR IN A MICROCANTILEVER AS A GAS SENSOR ..... 35

3.1 Transient Oscillator Behavior ..... 35
3.2 Damping ..... 36
3.3 Electrical Detection of Ringdown Behavior ..... 39
3.4 Numerical Model ..... 40
3.5 Gas Sensing ..... 41
3.5.1 Experimental Setup ..... 41
3.5.2 Experimental Results ..... 45

IV. RESONANCE IN CARBON NANOCOILS ..... 48

4.1 Properties of Carbon Nanocoils ..... 48
4.2 Synthesis Method for Carbon Nanocoils ..... 50
4.3 Experimental Setup and Approach ..... 50
4.4 Experimental Results ..... 55
4.5 Discussion ..... 63
4.5.1 Linear Results: Determination of the Lateral Spring Constant ..... 63
4.5.2 Nonlinear Behavior ..... 66

V. INTRINSIC DAMPING IN A MWNT ..... 69

5.1 Multi-Walled Carbon Nanotubes ..... 69
5.2 Sources of Damping in a Resonating MWNT ..... 70
5.3 Synthesis ..... 73
5.4 Experimental Results ..... 74
5.5 Discussion ..... 75

Table of Contents (Continued)

Page

APPENDICES ..... 80

A: Polar Representation of Resonance Peaks and Associated Calculations ..... 81
A.1 Polar Representation ..... 81
A.2 Quality Factor Determination ..... 83
B: Configuration of HDR Setup for use in an SEM ..... 86
C: Equipment List ..... 90

REFERENCES ..... 91

LIST OF TABLES

Table Page

3.1 Table 3.5.1: Densities and viscosities of mixtures of N2 and O2 based on both standard values and those observed by the electrical ring-down method. Good agreement with previously reported values and high specificity for the concentration are observed. ..... 47

4.1 Parameters of the cCNW observed to determine its material parameters ..... 60

LIST OF FIGURES

Figure Page

2.1 Theoretical electrical signal from a cantilever with resonant frequency of 15 kHz measured at ($Q_1$) the driving frequency, ($Q_2$) twice the driving frequency, and ($Q_3$) three times the driving frequency. The parasitic capacitance, creating the linear trend in $Q_1$ is not present at higher harmonics. ..... 23

2.2 Schematic of the system used to simultaneously measure electrical output and mechanical motion of the oscillating cantilever. The position detector is also connected to a Lock-In amplifier to measure the motion at various harmonics of the driving frequency, $V_{ac}$ ..... 27

2.3 Observed mechanical motion of the microcantilever at (a) the first, (b) second, and (c) third harmonic of the driving frequency. Black traces give theoretical fits based on equations for the motion of the cantilever. (Inset) Polar plots showing the circular behavior of the resonance peak ..... 28

2.4 Observed electrical signal of the microcantilever through HDR at (a) the first, (b) second, and (c) third harmonic of the driving frequency. (d) The smaller peaks at $\omega/2$ and $\omega/3$ in the third harmonic. (Insets) Polar plots of the same. The improved signal to background ratio at higher harmonics beyond the first can be clearly seen. In addition, the limaçon behavior at the second and third harmonic is evident ..... 29

2.5 Limaçon behavior of the resonance at a driving frequency of $\omega_0$ observed electrically at the second harmonic for several different bias voltages. As the bias changes, the shape on the polar plot changes from a circle beginning at the origin, to a cardioid, to a circle centered on the origin ..... 31

List of Figures (Continued)

Figure Page

2.6 The shape of a resonant peak for positive α for (a) no Duffing, (b) critical Duffing, characterized by the strong asymmetry of the peak, and (c) strong Duffing, characterized by the bifurcation of stable solutions. The dashed red line represents the unstable solution, not observable in practice. The shape of the peak observed will depend on the direction of the applied frequency change, as shown by the black arrows ..... 33

3.1 Sample electrical output for the ringdown of the cantilever exposed to two different gases. The lower viscosity of Hydrogen is evident immediately due to the longer time it takes the signal to decay ..... 43

3.2 (Red diamonds) The observed electrical signal for the ringdown of the cantilever and (black line) the theoretical fit using $\beta_1$ and $\beta_2$ as fitting parameters. The good agreement between theory and experiment can be seen ..... 44

3.3 (Red dots) Values for the viscosity and density for the gases measured according to NIST standards. (Points with error bars) The values for the same parameters determined by the electrical ring-down method. Gases with similar density, such as $H_2$ and $D_2$, can be easily differentiated with a single measurement using this method as both parameters can be measured simultaneously. Previously, differentiation at this specificity for two different parameters could not be obtained with a single measurement ..... 46

4.1 SEM image of as prepared cCNW samples ..... 49

List of Figures (Continued)

Figure Page

4.2 Schematic of HDR setup using SU6600 SEM vacuum chamber. The FET is located inside the chamber (left side) ..... 52

4.3 (green) Raw data collected for cCNW (a) in the polar representation and (b) as a function of frequency. (red) The same data with a vector added (black line in a) to remove background. (c) The resonant peak can be more clearly observed as a function of frequency after this subtraction has been made ..... 54

4.4 The visual amplitude is shown by the red squares and the electrical amplitude by the green circles. As can be seen, the electrical peak closely matches the observed mechanical resonance, showing that the electrical signal does represent the mechanical motion ..... 57

4.5 SEM image of the cCNW driven (a) away from resonance, (b) at its first mode (~30 kHz) and (c) at its second mode (~190 kHz). The counterelectrode can be seen in the upper corner of (b), and the different mode shapes can be clearly observed between (b) and (c) ..... 58

4.6 Electrical output from the cCNW resonance at a driving voltage of 6V. The red points were for increasing frequency, the green for decreasing. The super-critical Duffing behavior and hysteretic effects can be clearly seen..... 59

4.7 SEM image of the combination mode. The stretching and compression of the cCNW can be seen on the left and right sides of the motion respectively ..... 60

4.8 SEM image of the circularly polarized mode. The counterelectrode is pictured on the left ..... 61

List of Figures (Continued)

Figure Page


4.9 Electrical signal in the (green) increasing and (red) decreasing frequency directions for the combination and circularly polarized resonances. The large, lower frequency peak is due to the combination mode. The asymmetry of this mode can be clearly seen, although there is no hysteresis. The small, high frequency mode is due to the circular polarization. Significant hysteresis can be seen between the forward and back directions ..... 62

5.1 SEM image of MWNT in close proximity to the W counterelectrode (left) out of resonance and (right) resonating at its first mode ..... 75

5.2 Electrical output of resonating MWNT for the same driving voltage (8V) taken an hour apart. The frequency can clearly be seen to drift. The shape of the peak, however, remains relatively constant ..... 76

5.3 Electrical output from the resonating MWNT for a driving voltage of 3V (bottom curve) increasing by 1V up to 8V (top curve). Hysteresis can be observed for 6V, 7V, and 8V driving voltage ..... 78

5.4 The quality factor of the observed resonance, driven at $\omega$. As the driving voltage increases, the quality factor can be seen to decrease irregularly ..... 79

A.1 Typical circular resonance behavior in ($A$, $\varphi$) polar coordinates. The point labeled O is off resonance and A is at the resonance peak. Points B and B` are used to determine the FWHM of the peak ..... 85

B.1 SU6600 Scanning Electron Microscope ..... 87

List of Figures (Continued)

Figure Page

B.2 Custom-built jig for manipulation of CCE setup. Three separate piezoelectric motors can be used to control the fine relative position of the cantilever and counterelectrode in each of the three spatial dimensions. Coarse positioning is achieved with the large gold colored screws, which move on tracks to change two spatial dimensions and 1 angular degree of freedom. The FET can be seen on the left hand mount, connected remotely to the preamplifier (not pictured).....88

B.3 External electrical setup for HDR experiments under vacuum. From top: monitor for use with controlling PC (not pictured) and dc bias unit, function generator and preamplifier power supply, lock-in amplifier.....89

# CHAPTER ONE

# INTRODUCTION

## 1.1 Introduction

The scale of scientific exploration and technological interest has moved to encompass more and more the very small. As scientific tools improve to study objects on the micrometer or even nanometer scale, new physics is constantly being discovered, which motivates the development of more precise instruments to study the new phenomena. Instrumentation has advanced so far, that not only can objects nanometers in size be reliably observed and studied, but complex, functional systems and devices can be built with fine detail on this scale.

Some of the most interesting materials to be utilized in these systems are nano-cantilevers. Because of their high aspect ratio, over 10,000:1 in the case of the longest MWNTs, and essentially one dimensional character, they are valuable tools for both pure scientific inquiry and as components in larger devices. Synthesis methods are continuously improving, making the study and use of both metallic and semiconducting nano-cantilevers increasingly commonplace. Thanks to their high yield stress and, in particular, the ease with which they can be driven to mechanical resonance, they have shown great promise over a wide range of platforms, including use as chemical mass and force sensors, high frequency signal generators, photodetectors, batteries, lasers, radios, and for energy storage and as a laboratory for one dimensions physics.

However, in order to be useful in any of these contexts, reliable methods to actuate the cantilever and, more critically, detect its response to actuation are needed. Purely

electrical actuation and detection methods allow for precise characterization of micro- and nano-cantilevers in both their mechanical and electrical properties.

This thesis presents such a purely electrical method for the actuation and detection of mechanical resonance in micro- and nano-cantilevers. After a presentation of the elastic theory and synthesis and characterization of the cantilevers used, this method, the harmonic detection of resonance (HDR) is examined in-depth, including a description of the electrical actuation and mechanical response of the cantilever. From this response, the measurement of the electrical signal, which is at the heart of the method, is examined in detail. I then present a variation of this method and its effective use as a real-time gas sensor. Finally, a pair of experiments are presented, utilizing HDR, which, while interesting in their own right, also display the versatility of this method. These include: the successful vibration of a coiled carbon nanowire (cCNW) and the calculation of its material properties from its resonance and the observation of amplitude sensitive damping in a MWNT.

## 1.2 Modern Nano-Cantilevers

Ever since the discovery of multi-walled carbon nanotubes (MWNT) by Iijima [1] in 1991, investigations of these and other nanocantilevers have increased exponentially. Successful synthesis of single-walled carbon nanotubes [2], metallic and semiconducting nanowires, and even more esoteric geometries including nanobelts [3], nanosprings [4], and coiled nanotubes [5] quickly followed over the next 2 decades, and it was quickly clear that they had a number of promising applications. While less sturdy than a doubly

clamped beam, they have seen greater use because of their relative ease of production, and the high responsivity to external stimulus.

Uses for nano-cantilevers in modern devices are virtually limitless. The zepto-gram mass sensor has at its core a nanocantilever. They have shown use in a large number of capacities including in textiles [6], and as nano-generators [7], and lasers [8]. They show incredible sensitivity in sensing, acting as high precision biological and chemical sensors [9], pressure sensors [10], and force sensors [11]. They have also shown promise in electronics, being used as electrical switches [12]. As these structures become cheaper and easier to mass produce, mesoscopic and macroscopic uses for these highly sensitive, highly versatile objects will continue to increase.

### 1.3 Nano-cantilever Excitation

One of the great advantages of nano-cantilevers as high sensitivity devices is the ease with which they can be driven to resonance. By applying a periodic force to a singly-clamped cantilever at or near the natural frequency of the cantilever, relatively large amplitude oscillations can be induced in the cantilever. As was shown with the advent of non-contact atomic force microscopy, the properties of these oscillations are highly sensitive to factors both internal and external. In fact, the sensitivity of particular modes of vibration in AFM is so high that cantilevers have been specifically designed to take advantage of them.

In particular, small external forces or the addition of mass will cause a measurable shift in the resonance frequency of the cantilever and larger forces can even cause

quantifiable changes in the shape of its resonance peak (i.e. its amplitude as a function of driving frequency). In addition, the high sensitivity to frequency allows nano-cantilevers to be “tuned” for specific purposes including, in the most amazing case, as functional radios [13].

The methods of actuating these cantilevers to resonance are varied. They can be piezoelectrically driven, wherein the mount holding the cantilever is resonated by a piezoelectric device. By applying an oscillating voltage to the piezoelectric device, it will drive the mount at the frequency of the voltage. The signal will be transduced through the mount and into the cantilever, where it can drive it to resonance at the natural frequency of the cantilever. This has the advantage of working with any well mounted cantilever, and not requiring any geometric considerations, as the proper excitation frequency should produce excitation of the desired mechanical mode.

Alternatively, the cantilever can be driven electrically. This method is generally preferred for cantilevers which conduct or hold charge because of the ease with which it can be implemented and because there is no need for extra mechanical elements, such as a piezoelectric device.

## 1.4 Electrical Actuation and Detection in Nanocantilevers

As was first observed by Poncharal *et al*. [14], metallic nanocantilevers can be actuated by an alternating electrical field, driving the cantilever at its resonant frequency. As the cantilever is conducting, it will acquire a charge opposite to that of the field source, causing an attractive force. As the field alternates, the cantilever will oscillate.

Using this method, Poncharal was able to observe, using a scanning electron microscope (SEM) the resonance of several modes of a MWNT. Also, by measuring the amplitude of the oscillation in the SEM, a rough estimate of the quality factor of the nanotube resonator was made. In addition, measuring static deflection created by a large direct voltage bias, controllable, high stress deformations could be created and observed. Since then, several other experiments have been done on a variety of different nanocantilevers using this same method [15, 16].

Because electrical actuation relies heavily on the electrical properties of the resonating structure, in particular the induction of charge onto the cantilever, it is intuitive to investigate the electrical properties of the cantilever through this actuation method, and indeed, to use the electrical properties of the cantilever to detect the mechanical resonance. Several methods have been used to measure the resonance of a nano-cantilever electrically, that is to say, measuring current entering or leaving the cantilever. While an electrical actuation method is not necessarily required for an electrical detection scheme, it does significantly simplify the design of a device and, as we shall she for capacitive detection, can cause the flow of current by itself, giving a natural candidate signal to try to observe and measure.

### 1.4.1 Piezoresistive and Piezoelectric Detection

Piezoresistive and piezoelectric detection methods rely on the change of electrical properties of the cantilever as a result of applied stress. For piezoresistive detection, the resistance of the cantilever changes as a function of applied stress and by measuring the

change in a current flowed through the cantilever, deflection can be sensed. For piezoelectric detection, the stress causes a separation of charge in the cantilever which can then be measured as a current [17]. Both of these methods require either extensive engineering of the cantilever, particularly in the case of piezoresistive devices such as the one shown in figure 1.1. Because these devices must be specially designed so as to produce a net change in either resistance or charge, these detection methods would be impractical to study the physical properties of a synthesized nanotube or nanowire, and are better suited for use in silicon devices. In addition, the ability to fabricate such devices is limited by the scale at which the metal wiring can be deposited, forcing this technology out of the nanometer scale we are concerned with.

### 1.4.2 Field Emission Detection

A novel method of detecting electrical resonance in some nanocantilevers is based on their capability of field-emitting electrons when exposed to an electric field. In particular, in a nanocantilever such as a MWNT, an electric field will induce electrons to be emitted from the free end of the nanotube creating an emission current. Resonance can be observed by noticing the change in current due to change in the field enhancement factor resulting from the motion of the nanotube. In fact, using precise time resolution, amplitude and frequency modulated signals can be broadcast to the nanotube which can then demodulate them. This is the basis for the nanotube radio [13]. However, despite this impressive display, the method is still limited to cantilevers which display effective field emission. In addition, the precision with which the motion of the cantilever can be

determined is limited, as the variation of field enhancement will be a second order effect for normal cantilever motion.

### 1.4.3 Capacitive Detection

When the cantilever moves in response to the applied electric field, the capacitance of the system changes. This change results in a change in the amount of charge on the cantilever and current flows. The current responding to this dynamic change of capacitance should increase with the amplitude of oscillation of the cantilever, leading to a straightforward method of detecting the resonance by simply observing the flow of electricity through connections to the cantilever [18]. However, as will be shown in Chapter 2, parasitic signals from the rest of the capacitive system, normally overwhelm the smaller signal of interest. The difficulty in dealing overcoming these parasitic signals has prevented the effective measurement of the dynamic signal. Despite this, because of its relative ease and direct one-to-one relationship with the motion of the cantilever, much work has been done to try to design devices to optimally preserve the capacitive signal [19, 20]. However, through careful filtering, components of the dynamic signal can be observed in regions where the background from the parasitic capacitance is several orders of magnitude smaller than in the normal case. Using the same geometric considerations which give rise to the parasitic capacitance, it is possible to observe the dynamic signal for nano-cantilevers as small as 10 nm in diameter or smaller.

These geometric issues will be dealt with generally, along with the physics of electrical actuation and capacitive detection in Chapter 2. Chapter 3 will present a

technique related to HDR, which utilizes pulsed electrical signals and under-damped mechanical signal decay as a detection scheme. An effective gas sensor will be presented using this method. Finally, Chapters 4, and 5 will address particular discoveries made using the full power of the detection technique developed in Chapter 2.

# CHAPTER TWO

# THE HARMONIC DETECTION OF RESONANCE METHOD

## 2.1 The Need for Harmonic Detection of Resonance

In this section, the general model for electrostatically driving cantilevers is developed. While it can be directly seen that driving conducting cantilevers in this way will lead to an electrical output depending directly on the motion of the cantilever, it will be shown that, in addition to this signal, a parasitic signal, due to capacitances inherent in the electronic setup, will create a large background signal, preventing direct measurement of this signal. Harmonic Detection of Resonance (HDR) will then be introduced to circumvent this parasitic capacitance.

### 2.1.1 Electrostatic Driving of Cantilevers

By placing an electric field in the vicinity of a conducting cantilever, an electrostatic force can be generated on the cantilever. This force will work to minimize the capacitance of the cantilever-counter-electrode (CCE) system. In general, this force will act in 3 dimensions over the entire cantilever. However, it has been shown using numerical studies [21] that the majority of charge stored in the cantilever when the system is charged is located in the tip. Furthermore, since this force will create a regular, repeatable motion in the cantilever, we can describe the relative motion of the cantilever from equilibrium with just 1 degree of freedom (DOF), $x$, which will, generally speaking, refer to the displacement of the tip from the equilibrium position in the absence of an

electric field. This capacitive force will depend on the geometry of the CCE system used, but it can be generally written as:

$$F_C = \nabla E = \nabla\, CV^2 = V^2\, \nabla C = V^2\, \frac{\partial C}{\partial x} \tag{2.1}$$

where $F_C$ is the capacitive force, $E$ is the energy of the capacitor, $C$ is the capacitance, and $V$ is the applied voltage. In the final equality we have adopted the 1DOF $x$ as mentioned above.

The resulting change in capacitance will change the total charge on the capacitor as:

$$Q = CV \tag{2.2}$$

If an alternating voltage, $V_{ac}$, with dc bias, $V_{dc}$, is used to drive the cantilever at frequency $\omega$,

$$V = V_{dc} + V_{ac} \cos \omega t \tag{2.3}$$

the motion of the cantilever will produce a current as the capacitance changes and the total charge fluctuates. However, the oscillating voltage will also produce a current *I*, which will scale linearly with the frequency, creating a parasitic signal.

$$I = \frac{dQ}{dt} = \frac{d(CV)}{dt} = \frac{dC}{dt}V + \frac{dV}{dt}C = \frac{dC}{dt}(V_{dc} + V_{ac}\cos\omega t) - \omega C V_{ac}\sin\omega t \quad (2.4)$$

At resonance, the derivative in the first term should be large as the geometry changes rapidly. However, in practice, the parasitic signal, the second term, proportional to $\omega$, is much larger than the dynamic capacitive signal associated with the motion of the cantilever, making it normally unobservable in real experiments.

Let us examine the driving force in more detail. Substituting Eq 2.3 into Eq. 2.1, we find the force, as derived above will have frequencies at both $\omega$ and $2\omega$

$$F_C = \frac{dc}{dx}(\mathrm{V}_{dc}^2 + \mathrm{V}_{dc}\mathrm{V}_{ac}\cos\omega t + V_{ac}^2\cos^2\omega t) =$$

$$\frac{dc}{dx}\left(\mathrm{V}_{dc}^2 + \tfrac{1}{2}V_{ac}^2 + \mathrm{V}_{dc}\mathrm{V}_{ac}\cos\omega t + \tfrac{1}{2}V_{ac}^2\cos 2\omega t\right) \quad (2.5)$$

while the voltage oscillates only with frequency $\omega$. Reexamining Eq. 2.4, we can see that if we only observe signals at $2\omega$, the parasitic signal will not be present, while the dynamic signal will remain. This is the basis of the HDR method.

## 2.2 Characterization of HDR

This section will develop the mathematical theory behind the HDR method. First, the governing driving equation will be developed. This equation will them be solved approximately to give the actuated motion of the cantilever, using the method of harmonic balance. Then, the electrical signal predicted by this analysis will be calculated [22].

### 2.2.1 Equation of Motion for a Simple Harmonic Oscillator

Written in the displacement, *x*, we can write the equation of motion of a damped, driven, simple harmonic oscillator (SHO):

$$\frac{d^2x}{dt^2} + 2\gamma\frac{dx}{dt} + \omega_0^2 x = \frac{F(\omega,t)}{m} \tag{2.6}$$

where, $\gamma$ is the damping factor of the oscillator, $\omega_0^2=k/m$ is the square of the natural resonance frequency, $k$ is the spring constant and $m$ is the mass of the cantilever. In the case of a simple, periodic driving force

$$F = \cos\omega t \tag{2.7}$$

The periodic motion of the cantilever can be solved assuming a solution of the form

$$x(\omega, t) = A(\omega)\cos(\omega t + \varphi) \tag{2.8}$$

Plugging this into Eq. 2.6 above, we can solve for the amplitude and phase as a function of driving frequency:

$$A(w) = \frac{1}{\sqrt{\left(\omega_0^2 - \omega^2\right)^2 + (2\gamma\omega)^2}} \tag{2.9}$$

$$\tan\varphi(\omega) = \frac{2\gamma\omega}{\omega^2 - \omega_0^2} \tag{2.10}$$

There also exists the possibility of a solution that is not periodic in w. However, the magnitude of these solutions will decay to zero with a time constant of approximately $1/\gamma$. In chapter 3 we shall deal more with transient solutions to the force equation above, but for now, we shall only consider the periodic solutions, noting that any observations can be made after sufficient time for the transient solutions to have died off.

We also mention here that a polar plot of ($A$, $\varphi$) will be a circle (see appendix A). This will be particularly relevant when we examine experimental data looking for resonance peaks. While significant noise or background signals may distort the appearance of $A$ or $\varphi$ individually as a function of $\omega$, the circular pattern in the polar plot

will remain, confirming the existence of the resonance. It will also be of interest when we explore the consequences of our HDR theory and see deviations from this behavior.

### 2.2.2 Equation of Motion of HDR

For our driven cantilevers, the force equation is

$$\frac{d^2x}{dt^2} + 2\gamma\frac{dx}{dt} + \omega_0^2 x = \frac{F_C}{m} \tag{2.11}$$

where $F_C$ is the capacitive force given in Eq. 2.5. To attempt to solve this equation, we will first write the capacitance as a Taylor expansion in the displacement of the cantilever.

$$C(x) = C_0 + xC_1 + \frac{x^2C_2}{2} + \frac{x^3C_3}{6} + \cdots \tag{2.12}$$

where $C_n = d^nC/dx^n|_{x=0}$. So the force, $F_C$ becomes

$$F_C = \frac{1}{2}\left(C_1 + xC_2 + \frac{x^2C_3}{2} + \cdots\right)$$

$$\left[\frac{1}{2}V_{ac}^2 + V_{dc}^2 + 2V_{dc}V_{ac}\cos(\omega t) + \frac{1}{2}V_{ac}^2\cos(2\omega t)\right] \tag{2.13}$$

Plugging this force into Eq. 2.11, the equation becomes intractable. Even if the capacitance is truncated after a finite number of terms, the cantilever will still be driven by several forces at different frequencies, the amplitudes of which depend on the displacement. This makes the equation highly nonlinear and difficult to solve by normal calculus methods. However, using the solution of the simple harmonic oscillator as a guide and making several approximations, borne out by experiment, we can reduce this nonlinear, 2nd order differential equation to a set of coupled algebraic equations.

### 2.2.3 Simplifying approximations and the method of harmonic balance

To solve Eq. 2.11 we will first truncate our expansion of $C$ after three terms, assuming that $C_{n+1}x \ll C_n$ for the amplitudes of oscillation involved. That is to say, the capacitance expansion converges quickly over the scale of amplitudes of vibration. We then employ the method of harmonic balance and assume the solution takes the form:

$$x(\omega,t) = \sum_{n=0}^{\infty} x_n(\omega,t) \equiv \sum_{n=0}^{\infty} A_n \cos(n\omega t + \varphi_n) \qquad (2.14)$$

where $x_n$ is the motion of the cantilever at frequency $n\omega$, $A_n$ is the amplitude of that motion and $\varphi_n$ is the phase relative to the driving signal. Again any other motion will be transient and should die off exponentially with time constant $1/\gamma$. We must, for now, be willing to include terms arbitrarily large in $n$, because of the nonlinear nature of the equation; however, assumption #1 below will truncate the range of $x_n$ we need to explore. Notice also that we do not dismiss the possibility of a static displacement ($A_0$), moving

the cantilever, on average, closer to the counter-electrode. Because the cosine functions are orthogonal to each other, we can isolate terms based on their frequency and solve those algebraic equations for $x$ and $\varphi$ individually. Substituting into equation 2.13 we employ trigonometric identities to write equations that are linear in cos ($n\omega t$). However, this results in over a dozen terms for our equation at frequency $\omega$, almost 50 terms for $2\omega$, and over a staggering 100 terms for $3\omega$. In addition, these equations are coupled, with $A_1$ depending on $A_2$ and vice versa, but also nonlinear. In order to simplify these equations, we will make the following assumptions.

1. $A_n << A_m$ for $m>n$

2. $C_{n+1}A_m << C_n$ for all $m$, $n$

3. $A_n A_m = 0$ for $m \neq n$

As will be shown below, all of these assumptions are borne out by experiment under normal conditions. The one notable possible exception to these (assumption #2) will be explored below. After eliminating the terms made negligible by these approximations, we are left with 4 algebraic equations, with only the smaller amplitudes ($A_2$, $A_3$) depending on larger ones, effectively decoupling them:

$$A_0\omega_0^2 = \frac{1}{m}(A_0C_2+C_1)\left(\frac{1}{2}V_{ac}^2+V_{dc}^2\right) \tag{2.15}$$

$$A_1(\omega_0^2-\omega^2)\cos(\omega t+\varphi_1)+2A_1\gamma\omega\sin(\omega t+\varphi_1) =$$

$$\frac{1}{m}\left[\frac{1}{2}A_1V_{ac}^2C_2\cos(\omega t+\varphi_1)+A_1V_{dc}^2C_2\cos(\omega t+\varphi_1)+2V_{ac}V_{dc}C_1\cos(\omega t)\right] \tag{2.16}$$

$$A_2(\omega_0^2-4\omega^2)\cos(2\omega t+\varphi_2)+4A_2\gamma\omega\sin(2\omega t+\varphi_2) =$$

$$\frac{1}{m}\begin{bmatrix} A_2C_2\left(\frac{1}{2}V_{ac}^2+V_{dc}^2\right)\cos(2\omega t+\varphi_2)+ \\ V_{ac}^2C_1\cos(2\omega t)+A_1V_{ac}V_{dc}C_2\cos(2\omega t+\varphi_1)\end{bmatrix} \tag{2.17}$$

$$A_3(\omega_0^2-9\omega^2)\cos(3\omega t+\varphi_3)+6A_3\gamma\omega\sin(3\omega t+\varphi_3) =$$

$$\frac{1}{m}\begin{bmatrix} A_3C_2\left(\frac{1}{2}V_{ac}^2+V_{dc}^2\right)\cos(3\omega t+\varphi_3)+ \\ \frac{1}{4}A_1C_2V_{ac}^2\cos(3\omega t+\varphi_1)+A_2C_1V_{ac}V_{dc}\cos(3\omega t+\varphi_2)\end{bmatrix} \tag{2.18}$$

We will at this point notice that $A_0$ is, in fact, non-zero. However, we are free at this point to redefine the zero of our displacement, x, around this new equilibrium position. This will eliminate its influence from higher order equations. We notice that each of these equations (2.15-2.18) has two similar terms which will act to reduce the effective spring constant of the oscillator. We define $\omega_0{`}^2 = \omega_0^2 - m^{-1} C_2 (½V_{ac}^2 + V_{dc}^2)$ as the new resonant frequency to simplify the equations. We notice the effect these terms is

to reduce the natural frequency of the oscillator. This "spring softening" has been observed previously in the electrostatic resonance of microcantilevers [23]. In fact, as we shall see later, because of the voltage dependence on $\omega_0$`, we can tune the resonant frequency of the cantilever by changing the magnitude of the driving voltage. We also note that we can continue this process for $A_4$, $A_5$, etc. However, because the assumptions made above prevent these variables from affecting those in the equations above, we will stop at the 3rd harmonic of the driving frequency. There will, however, be peaks at these frequencies, both in the physical and electrical signal and they have been observed experimentally [23, 24].

Eqs. 2.16-2.18 can be solved in a straight forward, if tedious, manner:

$$A_1(\omega) = \frac{2C_1V_{dc}V_{ac}}{m\sqrt{\left(\omega_0'^2-\omega^2\right)^2+(2\gamma\omega)^2}} \tag{2.19}$$

$$\tan\varphi_1(\omega) = \frac{2\gamma\omega}{\omega^2-\omega_0'^2} \tag{2.20}$$

$$A_2(\omega) = \frac{V_{ac}}{m}\sqrt{\frac{(C_2A_1V_{dc})^2+\frac{1}{4}(C_1V_{ac})^2+C_1C_2V_{dc}V_{ac}\cos\varphi_1}{\left(\omega_0'^2-4\omega^2\right)^2+(4\gamma\omega)^2}} \tag{2.21}$$

$$\tan\varphi_2(\omega) = \frac{C_1 V_{ac}\sin\varphi_2' + 2C_1 A_1 V_{dc}\sin(\varphi_2' + \varphi_1)}{C_1 V_{ac}\cos\varphi_2' + 2C_1 A_1 V_{dc}\cos(\varphi_2' + \varphi_1)} \tag{2.22}$$

$$\tan\varphi_2'(\omega) = \frac{4\gamma\omega}{4\omega^2 - \omega_0'^2} \tag{2.23}$$

$$A_3(\omega) = \frac{V_{ac}}{m}\sqrt{\frac{\frac{1}{4}(C_2 A_1 V_{ac})^2 + 4(C_2 A_2 V_{dc})^2 + 2C_2^2 A_1 A_2 V_{dc} V_{ac}\cos(\varphi_1 - \varphi_2)}{\left(\omega_0'^2 - 9\omega^2\right)^2 + (6\gamma\omega)^2}} \tag{2.24}$$

$$\tan\varphi_3(\omega) = \frac{\frac{1}{2}A_1 V_{ac}\sin\varphi_3' + 2A_2 V_{dc}\sin(\varphi_3' + \varphi_1 - \varphi_2)}{\frac{1}{2}A_1 V_{ac}\cos\varphi_3' + 2A_2 V_{dc}\cos(\varphi_3' + \varphi_1 - \varphi_2)} \tag{2.25}$$

$$\tan\varphi_3'(\omega) = \frac{6\gamma\omega}{9\omega^2 - \omega_0'^2} \tag{2.26}$$

where we have introduced $\varphi_2$` and $\varphi_3$` , the phases of the oscillation ignoring the contributions from $x_1$ and $x_2$ respectively, for ease of notation and also to provide insight into the source of the components of the output.

As noted in Eq. 2.2, we can calculate the charge on the cantilever, and, differentiating, the current which will give our electrical signal. Separating as before into

harmonics and again assuming $C_n >> A_m C_{n+1}$, neglecting the smaller terms if they have the same phase, we have

$$Q_1 = \left[C_0 + \frac{1}{4}(A_1^2 + A_2^2 + A_3^2)C_2\right] V_{ac}\cos(\omega t) +$$

$$A_1 C_1 V_{dc}\cos(\omega t + \varphi_1) + \tfrac{1}{2} A_2 C_1 V_{ac}\cos(\omega t + \varphi_2) +$$

$$\tfrac{1}{8} A_1^2 C_2 V_{ac}\cos(\omega t + 2\varphi_1) \qquad (2.27)$$

$$Q_2 = \frac{1}{2} A_1 C_1 V_{ac}\cos(2\omega t + \varphi_1) + A_2 C_1 V_{dc}\cos(2\omega t + \varphi_2) +$$

$$\frac{1}{2} A_3 C_1 V_{ac}\cos(2\omega t + \varphi_3) + \frac{1}{4} A_1^2 C_2 V_{dc}\cos(2\omega t + 2\varphi_1) +$$

$$\tfrac{1}{48} A_1^3 C_3 V_{ac}\cos(2\omega t + 3\varphi_1) \qquad (2.28)$$

$$Q_3 = \frac{1}{2} A_2 C_1 V_{ac}\cos(3\omega t + \varphi_2) + A_3 C_1 V_{dc}\cos(3\omega t + \varphi_3) +$$

$$\frac{1}{8} A_1^2 C_2 V_{ac}\cos(3\omega t + 2\varphi_1) + \frac{1}{8} A_2^2 C_2 V_{ac}\cos(3\omega t + 2\varphi_2) +$$

$$\tfrac{1}{24} A_1^3 C_3 V_{dc}\cos(3\omega t + 3\varphi_1) \qquad (2.29)$$

We note here that including terms of higher order in the capacitance will distort the form of the observed resonant peaks, but will not generate any new ones; also, since we include the higher order terms with different phases, we will be able to see any interesting structure in the resonance.

### 2.2.4 Features of Our Solution

We note in both the physical amplitudes, $A_n$, and in the electrical charge $Q_n$, there will be several peaks depending on the harmonic examined and the frequency supplied to the cantilever. As expected, the cantilever will resonate when driven by a signal at its natural frequency, exactly analogous to the SHO, but also at half of this frequency, due to the frequency doubling of the force described above. In addition, because of the nonlinearity in the system, the cantilever will also be excited to resonance at its natural frequency when driven at one third this frequency (and at 1/4, 1/5, 1/6 etc.). This is not particularly surprising as the electrostatic force is the product of several terms each depending on the driving frequency, causing frequency doubling, tripling, and more. What is unusual is that, due to the recursive nature of the equations for the $A_n$s, $A_2$ has a peak when $A_1$ does, and $A_3$ has a peak when $A_1$ and $A_2$ do. This means that the cantilever will be excited at frequencies other than its natural frequency. This is a purely nonlinear effect which significantly complicates the cantilever motion.

We further note here that including terms of higher order in the capacitance will distort the form of the observed resonant peaks, but will not generate any new ones; also, since we include the higher order terms with different phases, we will be able to see any

interesting structure in the resonance. Figure 2.1 shows $Q_1$, $Q_2$, and $Q_3$, plotted on an arbitrary scale, to aid the reader in the following discussion. Examining the electrical current (= $dQ/dt$) output for the first harmonic, term by term, we see that at the input frequency there is a "dynamic" component, proportional to $A_1$, which should appear as a normal resonance, and a parasitic component, proportional to $C_0$, which, because the factor of $\omega$ in the current, will increase with frequency. There is also a term which looks like the second harmonic of the motion of the cantilever, although this should be difficult to see on top of the parasitic signal. There are also terms in phase with the parasitic signal, which may distort the peak at $\omega$ and $\omega/2$, but should have no other effect. The term proportional to $A_1$ is similar to another term in the second harmonic, and we will consider its effects shortly. Though this term is relatively small, it should have a similar effect, if diminished, to the term in the second harmonic.

At the second harmonic of the input frequency $2\omega$ there is no parasitic component in the output. Instead, there are only terms proportional to the mechanical amplitudes, with no constant terms which alter the output. This is also the case for the third harmonic. Using the information about the mechanical motion given above, details about the current flowing from the resonating structure can be found. At the second harmonic of the driving frequency, we expect peaks at $\omega = \omega_0/2$ and $\omega = \omega_0$. At $\omega = \omega_0/2$, $A_1$ is vanishingly small, so only $A_2$ should contribute to the current, and the peak should be similar in form to the same peak in $A_2$, which should be Lorentzian, as demonstrated previously.

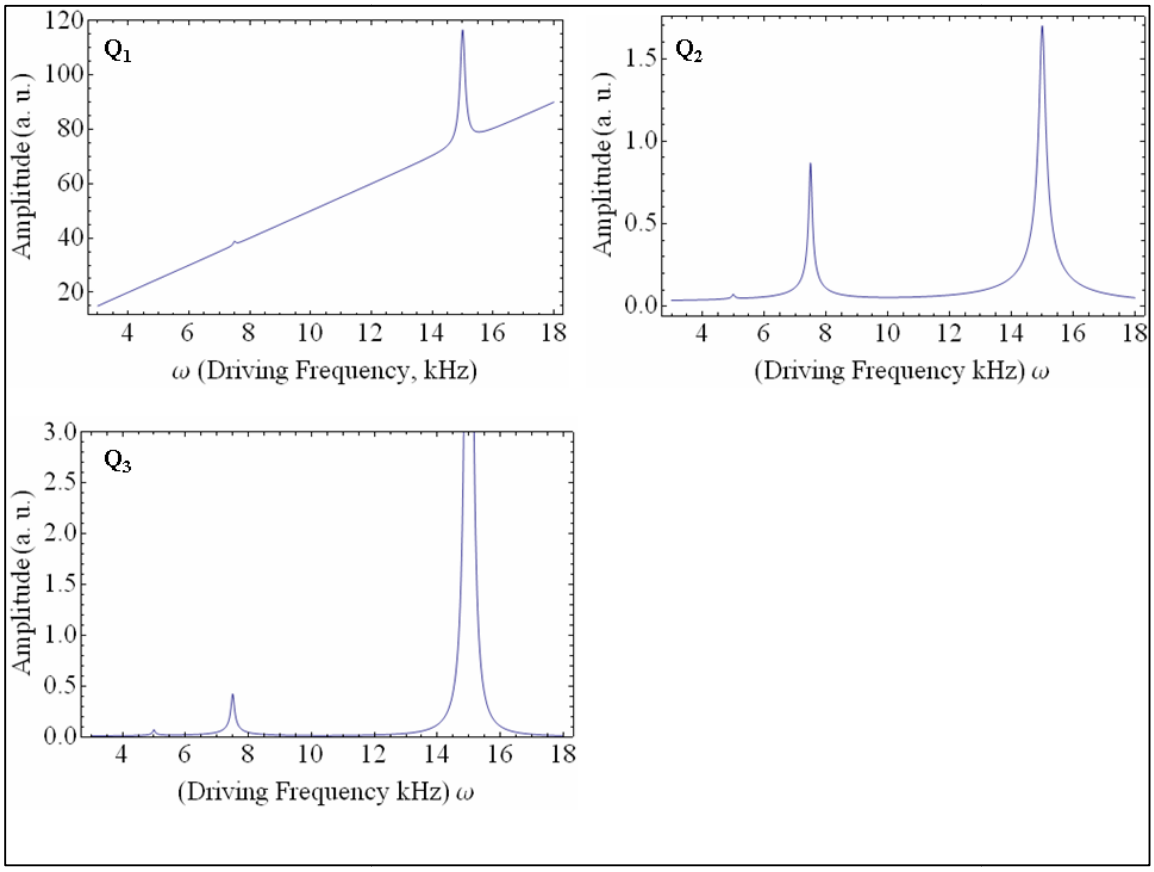


Figure 2.1: Theoretical electrical signal from a cantilever with resonant frequency of 15 kHz measured at ($Q_1$) the driving frequency, ($Q_2$) twice the driving frequency, and ($Q_3$) three times the driving frequency. The parasitic capacitance, creating the linear trend in $Q_1$ is not present at higher harmonics.

2.2.5 Anomalous Limaçon behavior

At $\omega=\omega_0$, however, we will see contributions from three components, proportional to powers of $A_1$, each having a phase shift relative to the others (similar to the peak in the first harmonic). For our purposes, we will ignore the term proportional to $A_1^3$, as it should be at least an order of magnitude smaller than the first two. We will assume these two terms dominate any small resonance at $\omega_0$ due to $A_2$. Using polar coordinates, as we did to identify the circle for the SHO and then transforming to Cartesian ones ($\zeta$ and $\xi$, to avoid confusion with the $x$ used above), it can be seen that the complex output amplitude will closely resemble a limaçon [25] offset by a constant along the $\zeta$-axis.

$$\zeta(\omega) = \frac{1}{2}\left[C_1 A_1 V_{ac}\cos\varphi_1 + \frac{C_2}{2}A_1^2 V_{dc}\cos 2\varphi_1\right] =$$

$$\frac{1}{2}\left[C_1 A_1 V_{ac}\cos\varphi_1\left(1+\frac{C_2 A_1 V_{dc}}{C_1 V_{ac}}\cos\varphi_1\right) - \frac{C_2}{2}A_1^2 V_{dc}\right] \qquad (2.30)$$

$$\xi(\omega) = \frac{1}{2}\left[C_1 A_1 V_{ac}\sin\varphi_1 + \frac{C_2}{2}A_1^2 V_{dc}\sin 2\varphi_1\right]$$

$$= \frac{1}{2}\left[C_1 A_1 V_{ac}\sin\varphi_1\left(1+\frac{C_2 A_1 V_{dc}}{C_1 V_{ac}}\cos\varphi_1\right)\right] \qquad (2.31)$$

The result is that for values of the input parameters where the two terms are approximately equal in magnitude, the amplitude will decrease sharply around the mechanical resonance as they interfere destructively with each other.

For the third harmonic of the output signal $3\omega$ we again expect nearly Lorentzian peaks around $\omega=\omega_0/3$ and $\omega=\omega_0/2$, from the term proportional to $A_3$ and $A_2$ respectively. At $\omega=\omega_0$, the curve will be complicated in a manner similar to that above, driven by terms that peak at the same value, but with varying phases. At certain points along the resonance, the terms will interfere constructively, at some points, destructively.

## 2.3 Experimental Verification of HDR

In order test the predictions of our model above, a CCE geometry was constructed in an Atomic Force Microscope (AFM) with an AFM cantilever used as the cantilever to be resonated, as reported previously [22]. The schematic for the electrical setup can be seen in Figure 2.2. It is comprised of a silicon microcantilever (Mikromasch NSC12 series, cantilever E with approximate dimensions 350 μm x 35 μm x 2 μm) which is driven into resonance using a relatively shorter microcantilever (Mikromasch NSC12 series, cantilever B with approximate dimensions 90 μm x 35 μm x 2 μm) as the counter electrode. Since the resonant frequencies of the long and short cantilevers were ~15.5 kHz and 300 kHz respectively, input frequencies in the range of the long cantilever's resonance should not influence the mechanical motion of shorter cantilever. A function generator and a variable applied dc bias were used to charge the counter electrode. The cantilever used for measurement was then placed in an Atomic Force Microscope (AFM, Veeco CP-II), so the displacement of the cantilever tip could be measured, and also connected electrically to an operational amplifier (Amptek, A250) whose output was connected to a lock-in amplifier, the output of which is our measured the electrical signal.

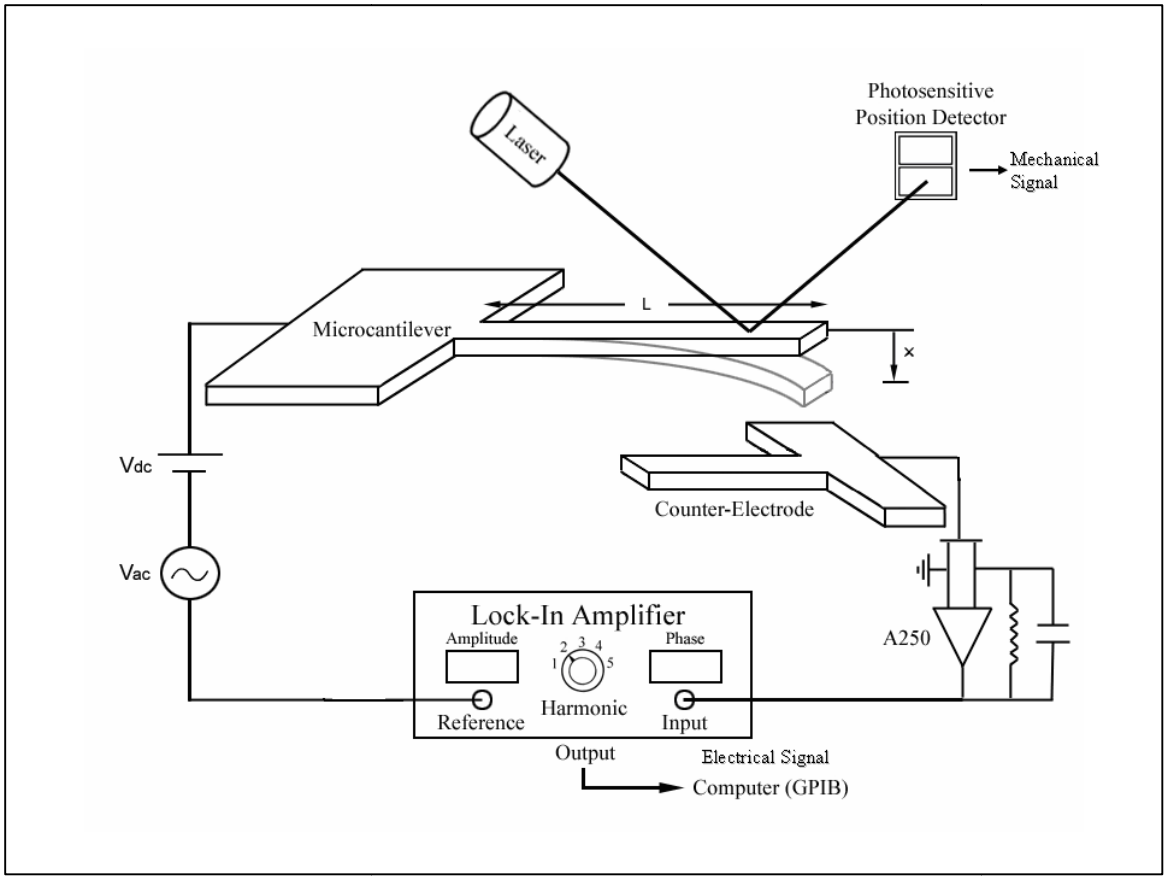


Figure 2.2: Schematic of the system used to simultaneously measure electrical output and mechanical motion of the oscillating cantilever. The position detector is also connected to a Lock-In amplifier to measure the motion at various harmonics of the driving frequency, $V_{ac}$.

The displacement signal from the AFM is also connected to a separate lock-in, so the mechanical oscillation and the electrical output could be measured independently and concurrently. The cantilevers were aligned in a parallel plate arrangement, and separated by a distance of ~10 μm. Measurements were taken at ambient conditions and only the first mode of vibration of the microcantilever is examined in detail in this study.

Figure 2.3 shows the physical amplitude of vibration at each of the first 3 harmonics, along with a fit using Eqs. 2.19, 2.21, and 2.24 above with the constants $C_1$,$C_2$, etc., the damping $\gamma$, and $\omega$ as the fitting parameters. As can be seen, good agreement is found between the two. In addition, using the relative phase of the motion, the circular polar behavior of the first 2 harmonics can also be seen.

Figure 2.4 shows the electrical signal from the same cantilever for the first 3 harmonics of the driving frequency. All of the salient features predicted above can be seen, including the parasitic and partially obscured dynamic signal in the first harmonic as well as the multiple, clear peaks evident in the 2$^{nd}$ and 3$^{rd}$ harmonics. Of particular note is the variation in signal-to-noise ratio in the 3$^{rd}$ harmonic, clearly much higher in the electrical signal.

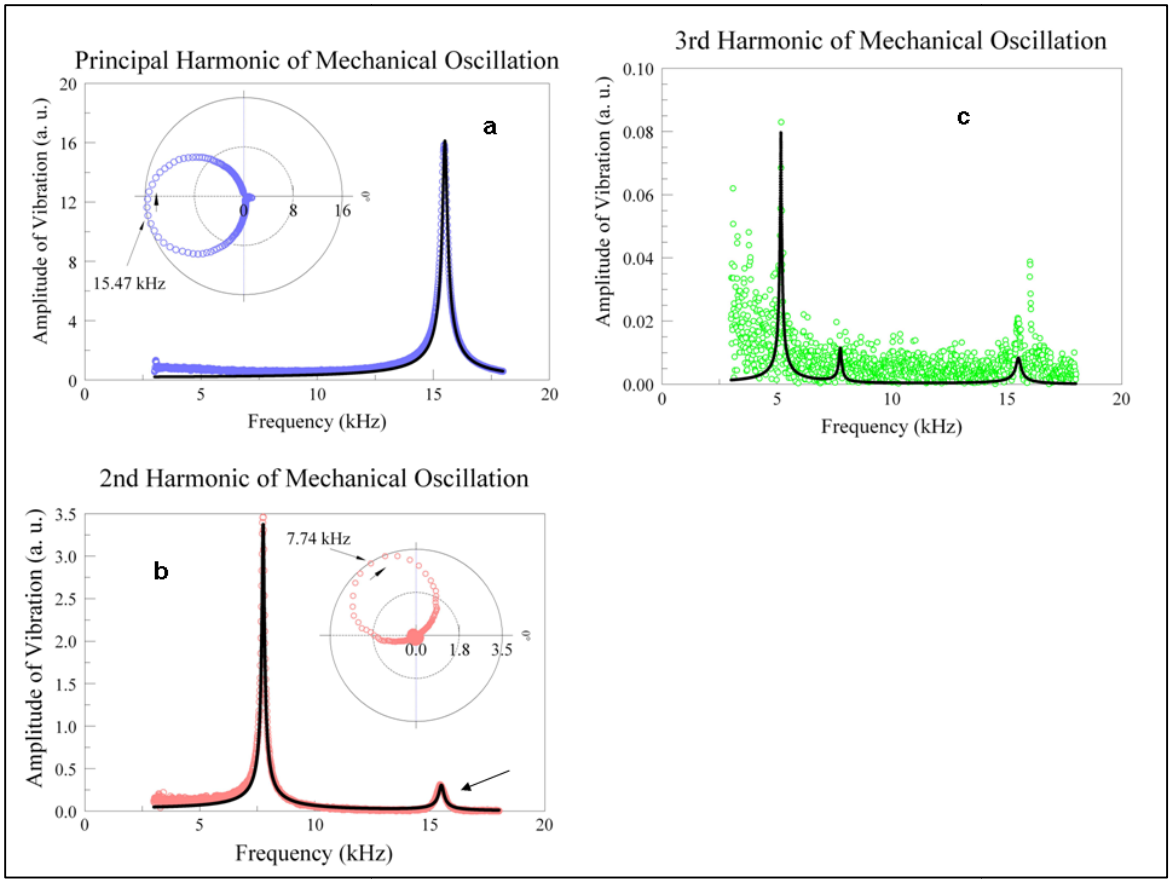


Figure 2.3: Observed mechanical motion of the microcantilever at (a) the first, (b) second, and (c) third harmonic of the driving frequency. Black traces give theoretical fits based on equations for the motion of the cantilever. (Inset) Polar plots showing the circular behavior of the resonance peak.

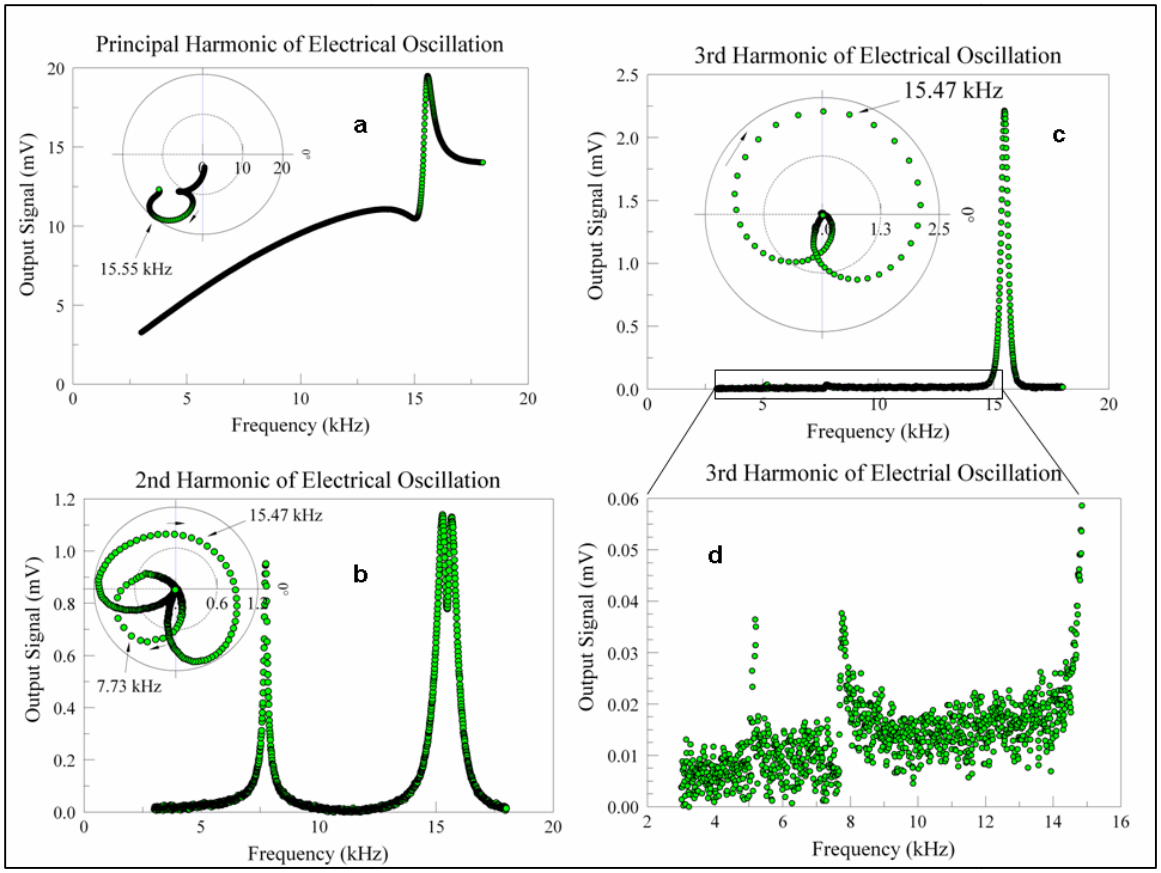


Figure 2.4: Observed electrical signal of the microcantilever through HDR at (a) the first, (b) second, and (c) third harmonic of the driving frequency. (d) The smaller peaks at $\omega/2$ and $\omega/3$ in the third harmonic. (Insets) Polar plots of the same. The improved signal to background ratio at higher harmonics beyond the first can be clearly seen. In addition, the limaçon behavior at the second and third harmonic is evident.

Figure 2.5 shows the polar plots of the experimental electrical resonance at $\omega=\omega_0$ for the second harmonic at varying dc voltages. As noted above, this peak should closely resemble a limaçon. We see, as the dc voltage increases, the curve changes from a circle (a normal resonance peak), to a cardioid, and eventually to a circle centered on the origin, where the resonance can no longer be seen in the amplitude plot. This agrees well with the theoretical model given above. One will notice that, when the cancellation between the two signals is largest, the amplitude change occurs very rapidly, more rapidly than anywhere else in the spectrum. This change in amplitude could be useful in various sensing applications, where a shift in the amplitude is measured. Because the change in amplitude is so great, smaller changes in the resonant frequency can be accurately measured, allowing for greater sensitivity.

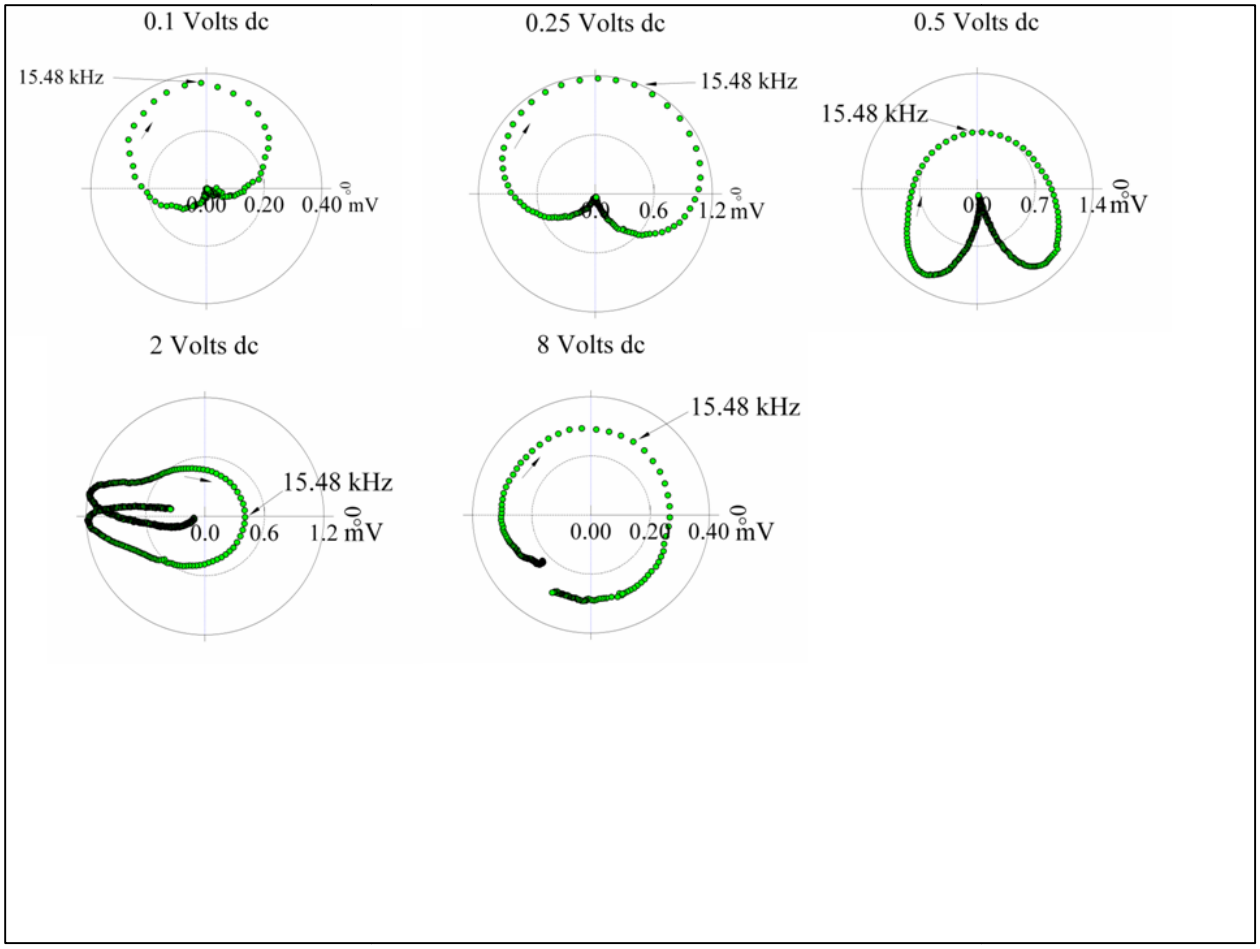


Figure 2.5: Limaçon behavior of the resonance at a driving frequency of $\omega_0$ observed electrically at the second harmonic for several different bias voltages. As the bias changes, the shape on the polar plot changes from a circle beginning at the origin, to a cardioid, to a circle centered on the origin.

## 2.4 Nonlinear Behavior

While the approximations made earlier made possible the solutions for the physical and electrical amplitudes which match the observed experimental evidence, there are a number of situations, readily observable in various HDR experiments where at least one of these assumptions fails. Assumptions 1 and 3 are in place to decouple Eqs 2.15-2.18 and, were they to fail, it would create substantial back-action, causing our solutions to become coupled, which may give rise to additional peaks in $A_1$ or $A_2$, or create small deviations in their lineshape, which have not been yet observed in any HDR experiment. Assumption 2, however, exists to linearize the equations. If terms of the form $A_1^3$ are allowed to remain, the EOM of the amplitudes $A_n$ will resemble Duffing's equation [24]:

$$\frac{d^2x}{dt^2} + 2\gamma\frac{dx}{dt} + \omega_0^2 x + \alpha x^3 = \frac{F_c}{m} \tag{2.32}$$

What this means is that, depending on the sign of alpha, the resonant lineshape will be asymmetrically tilted towards either higher or lower frequencies. For the largest nonlinearities, due either to large amplitude or large $\alpha$, a bifurcation of stable solutions will actually occur (Fig. 2.6). In practice, this means that, depending on the direction the frequency is scanned from, the peak will have a different shape, staying on either the higher or lower branch, until it is forced, due to the lack of a stable solution at the driving frequency, to switch.

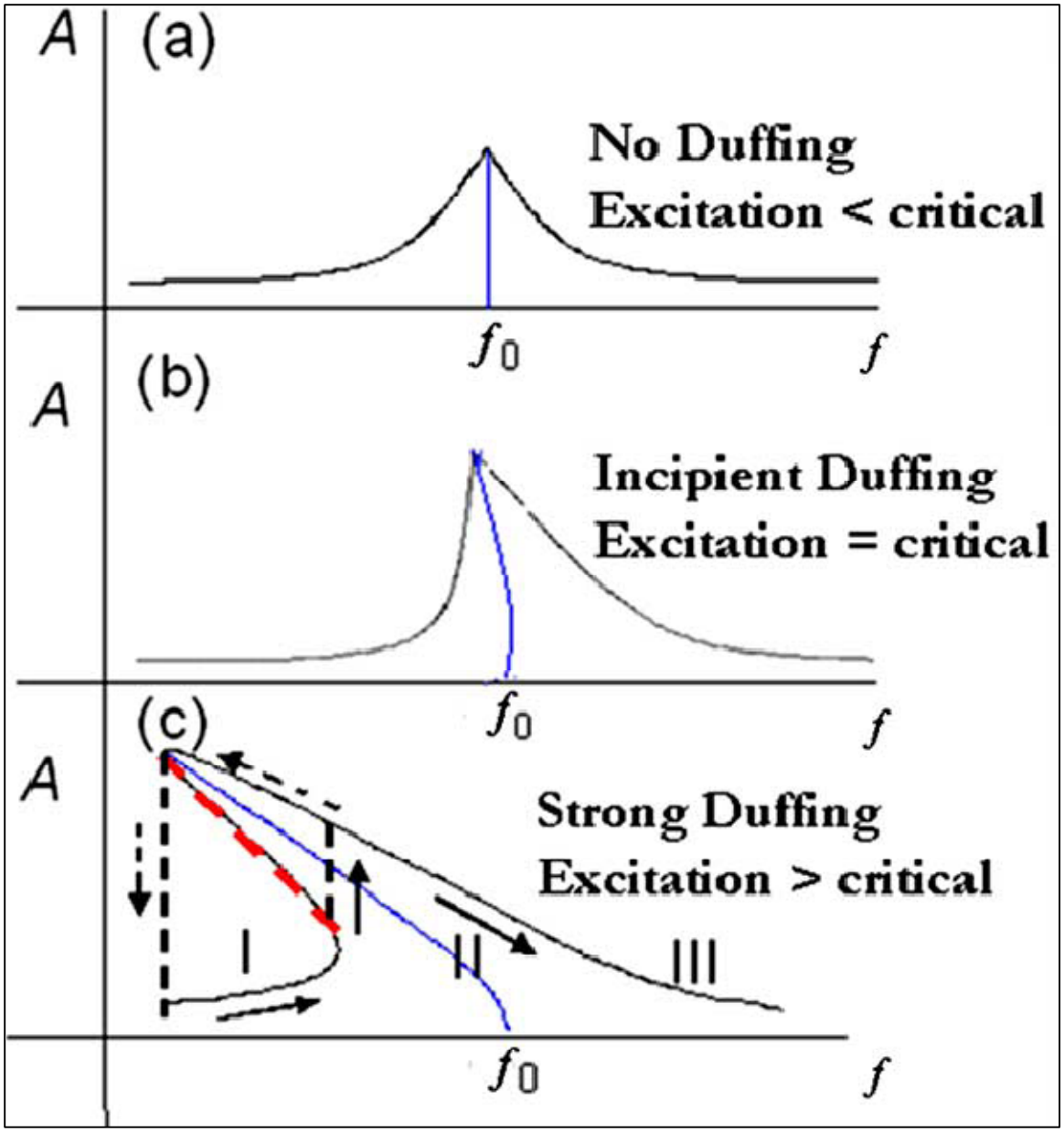


Figure 2.6: The shape of a resonant peak for positive α for (a) no Duffing, (b) critical Duffing, characterized by the strong asymmetry of the peak, and (c) strong Duffing, characterized by the bifurcation of stable solutions. The dashed red line represents the unstable solution, not observable in practice. The shape of the peak observed will depend on the direction of the applied frequency change, as shown by the black arrows.

Due to nonlinearities in the capacitance being essential to HDR (to see this, set $C_2$ and $C_3$ to zero in the equations above and notice how many peaks disappear), Duffing behavior is common at higher amplitudes as will be seen below, and has been studied in HDR systems in detail [24]. While this behavior can complicate data acquisition, the features of a resonance can still be easily approximated using the polar plot method from before. Moving through the resonance still results in a (nearly) circular trace. As shown in red in Fig 2.4.1, the unstable solution, never seen experimentally, for strong Duffing past the critical point simply corresponds to a missing arc of the circle in the polar plot. The full circle can still be interpolated and, from it, the peak frequency and quality factor can easily be determined.

# CHAPTER 3

# ELECTRICAL DETECTION OF RINGDOWN BEHAVIOR IN A MICROCANTILEVER AS A GAS SENSOR

## 3.1 Transient Oscillator Behavior

A novel variation of the HDR method exists using the ringdown of an undriven cantilever [26]. In order to investigate such an undriven system, the transient behavior of our oscillator must be examined. As mentioned previously, transient solutions to the harmonic oscillator equation will exist in addition to the periodic solutions utilized for HDR. These will be the solutions to the homogenous SHO equation:

$$\frac{d^2x}{dt^2} + 2\gamma\omega_0\frac{dx}{dt} + \omega_0^2 x = 0 \tag{3.1}$$

In the absence of any external driving force, the solution will take different forms depending on the damping parameter: $\gamma$. Depending on the solutions for the parameter, $\beta$, of the characteristic equation for the oscillator:

$$\beta^2 + 2\gamma\omega_0\beta + \omega_0^2 = 0 \tag{3.2}$$

There are three possible forms for the solution of the homogenous equation. For overdamping, where $\gamma > 1$, and Eq. 3.2 has 2 real solutions, the oscillator motion will be of the form

$$x(t) = Ae^{\beta_1 t} + Be^{\beta_2 t} \tag{3.3}$$

where $\beta_1$ and $\beta_2$ are the 2 solutions and $A$ and $B$ depend on the initial conditions. For critical damping where $\gamma$ =1, Eq. 3.2 has 1 solution and

$$x(t) = (A + Bt)e^{-\omega_0 t} \tag{3.4}$$

Finally, for underdamping, $\gamma$ <1, the solutions to 3.2 will be imaginary and

$$x(t) = \left(A\cos\left(\omega_0\sqrt{1-\gamma^2}\right) + B\sin\left(\omega_0\sqrt{1-\gamma^2}\right)\right)e^{-\gamma\omega_0 t} \tag{3.5}$$

For sufficiently small damping, by observing the ringdown behavior associated with Eq. 3.5, it is possible to extract both the resonant frequency, $\omega_0$ and the damping $\gamma$.

## 3.2 Damping

Damping in a cantilever structure typically comes predominately from 2 sources: intrinsic friction and interaction with its atmosphere. While the intrinsic friction can be very interesting for novel cantilevers (as will be seen later), at atmospheric pressure it is

much smaller than that due to the atmosphere. We will deal here predominately with that external damping from the environment.

The acceleration on our cantilever in a gaseous environment is typically written with 2 additional parameters [27]:

$$\frac{d^2x}{dt^2} = \left(-kx - (\beta_1 + c)\frac{dx}{dt} + F_C\right) / \left(m + \frac{\beta_2}{\omega}\right) \tag{3.6}$$

where $m$ is the effective mass, and $x$ is the position of the cantilever, $k$ is its spring constant, $F_C$ is the capacitive force as before, $c$ is the intrinsic damping in the cantilever, and $\beta_1$ and $\beta_2$ are the coefficients of the dissipative and inertial damping respectively. $\beta_1$ governs what is more commonly thought of as drag, dissipating energy from the cantilever into the gas. This drag will increase the damping of the cantilever, decreasing its amplitude and causing an undriven cantilever to relax to equilibrium. $\beta_2$ is due to the mass of the gas (or liquid) molecules which are moved along with the cantilever when it vibrates. As can be seen, the effect of this drag is to increase the effective mass of the cantilever, decreasing its natural frequency.

For a given geometry, calculation of the parameters $\beta_1$ and $\beta_2$ depends on the solution to the Navier-Stokes equation. Closed solutions to this equation are not known for arbitrary geometries, so for purposes of calculation the drag force, the cantilever is modeled as a series of spheres with diameter approximately equal to the width of the

cantilever and enough spheres such that their total length is approximately equal to the length of the cantilever. In this case, $\beta_1$ and $\beta_2$ are given by [27]:

$$\beta_1 = 6\pi\eta R\left(1 + {}^{R}/_{\delta}\right) \tag{3.7}$$

$$\frac{\beta_2}{\omega} = \frac{2}{3}\pi R^3\rho\left(1 + {}^{9}/_{2}\,{}^{\delta}/_{R}\right) \tag{3.8}$$

where $\eta$ is the viscosity of the gas, $R$ is the radius of the sphere, $\rho$ is the density of the fluid, and

$$\delta = \sqrt{{}^{2\eta}/_{\rho\omega}} \tag{3.9}$$

is the thickness of the boundary layer. It is important to note that the 2 independent characteristics of a gas which determine damping, namely its density and viscosity, can be calculated if one knows $\beta_1$ and $\beta_2$. It is also significant that $\beta_1$ and $\beta_2$ influence the motion of a cantilever in distinct ways, as mentioned above.

Assuming the cantilever is underdamped, it is possible, by measuring the ringdown of a cantilever to calculate $\beta_1$ and $\beta_2$ independently as fitting parameters to Eq. 3.5. As we will see below, we can use an electrical method, as before, to observe the

motion of the cantilever, and, from its ringdown, determine $\beta_1$ and $\beta_2$ and calculate $\eta$ and $\rho$.

3.3 Electrical Detection of Ringdown Behavior

The effects of gaseous environments on the quality factor and ringdown of microcantilever resonators has been considered previously [28-30]. However, electrical detection of this phenomenon adds increased capabilities for this technology. If we consider the electric charge on a cantilever as we did before, but now eliminate the external oscillating field, we find a current:

$$I(t) = \frac{dC}{dt} V_{dc} \tag{3.10}$$

So if the cantilever is in motion, it will produce an electrical signal without the parasitic capacitance (compare to Eq. 2.4). As shown above, in the case of the underdamped oscillator, this signal will oscillate and can persist for a great number of cycles. By driving the cantilever to resonance and then removing the external driving force, it is possible to observe the motion of the cantilever, and, in particular, its damping electrically. This is the basis for the ringdown detection method.

By assuming that the capacitance will be monotonic in the deflection of the cantilever, we can determine that, for a particular initial setup and geometry, there will be a one-to-one correspondence between the electrical output and the position of the

cantilever. If this relation is known, the deflection of the cantilever will be known through the electrical position.

## 3.4 Numerical Model

In order to determine the relation between electrical signal and physical deflection, we must first develop a numerical model to describe the capacitance of our cantilever counterelectrode system. The counterelectrode to be modeled was, as above, a sharpened Tungsten tip, and the cantilever was a silicon microcantilever (Mikromasch NSC12 series, cantilever B). The closest approximation to this system would be a conducting cone with its radial axis parallel to a conducting plane. However, a closed form for the capacitance of this system is not known in general. However, the capacitance of a wire parallel to a plane is known:

Using systems of this known capacitance, we can decompose the geometry into a system of wires of varying dimension parallel to a plane (see Fig 3.3.1), in order to approximate a conic shape. The resulting capacitance, $C_m$ is [26]:

$$C_m(r) = \frac{1}{2}\pi\varepsilon_0 L \sum_i \left(\cosh^{-1}\left(\frac{r}{r_i}+1\right)\right)^{-1} + C_S \qquad (3.11)$$

Where

$$C_s = 2\pi\varepsilon_0 r_1 \left(\frac{1+y-y^3}{1-y^2} + \frac{y^3}{1-2y^2} + \frac{y^4}{1-3y^2+y^4} + \frac{y^5}{1-4y^2+3y^4}\right) \qquad (3.12)$$

here, $r_i$ is the radius of the $i^{th}$ segment of wire, y = ½ $r_1$ / ($r_{eq}$+$r_1$), $\varepsilon_0$ is the permittivity of free space, $L$ is the length of a wire segment and $r$ is the distance of the wire from the plane. $C_s$ is the capacitance of a half sphere with the plane, used as a termination for the conical counterelectrode.

Now, knowing the total force on the cantilever, as a function of deflection, we can model its motion with $\beta_1$ and $\beta_2$ as free parameters, depending on the environment. Knowing the capacitance, it is also straightforward to determine the electrical signal as a function of amplitude, using Eq. 3.10 above which we can invert numerically to determine the position of the cantilever from the electrical signal.

## 3.5 Gas Sensing

As an application of this method of extracting the ringdown motion of the cantilever from the electrical signal, the sensitivity of the electrical signal to both parameters of the gaseous damping will be tested, along with its ability to identify unknown gases species or binary mixtures.

### 3.5.1 Experimental Setup

The electrical setup used was identical to that presented in Fig. 2.2, except in place of a lock-in amplifier, an oscilloscope was used to measure the output in time instead of frequency space. The CCE was placed in a vacuum chamber which could be filled to atmospheric pressure with the desired gas. The cantilever was driven to resonance to produce a high initial amplitude (higher than would be available from static

dc attraction alone) and then the ac signal was switched off, allowing the cantilever to relax to equilibrium. This process of excitation and relaxation was repeated at a frequency 10 Hz so sampling could be done to improve the signal-to-noise ratio. This sampling allowed the ringdown of the cantilever to be observed (Fig. 3.1).

The electrical output, averaged over several thousand cycles, could then be matched to the predicted output with good precision (Fig. 3.2) to determine the mechanical motion of the cantilever. From the mechanical motion, the two fitting parameters, $\beta_1$ and $\beta_2$ could be determined. As mentioned previously. As $\beta_1$ will primarily affect the lifetime of the oscillations while $\beta_2$ will affect the frequency of the oscillations, they can be effectively decoupled in the measurement.

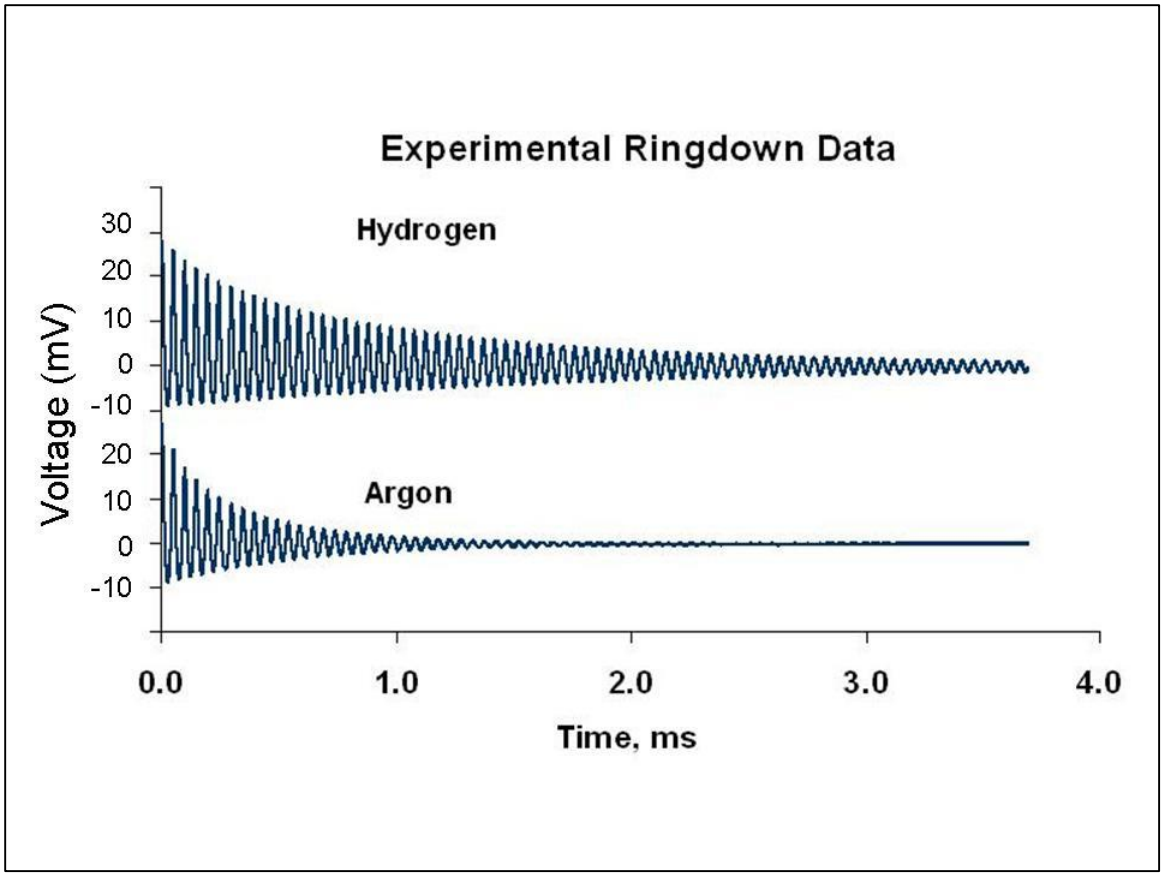


Figure 3.1: Sample electrical output for the ringdown of the cantilever exposed to two different gases. The lower viscosity of Hydrogen is evident immediately due to the longer time it takes the signal to decay.

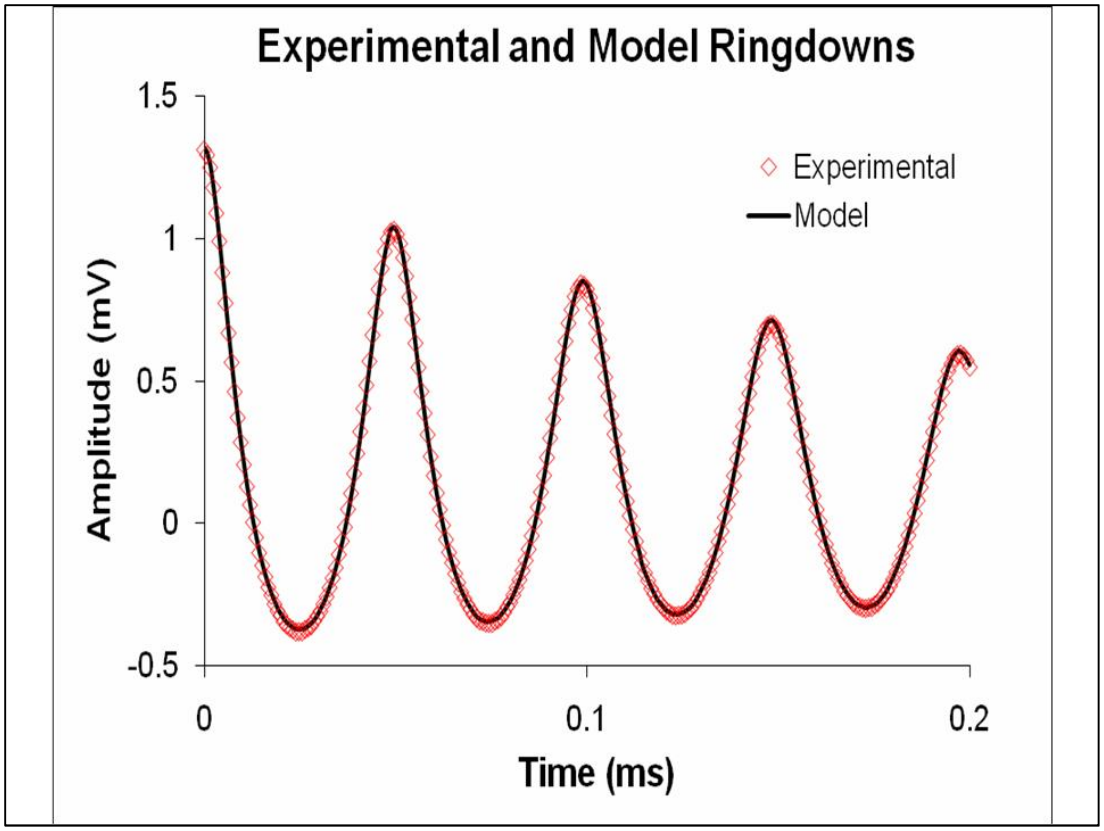


Figure 3.2: (Red diamonds) The observed electrical signal for the ringdown of the cantilever and (black line) the theoretical fit using $\beta_1$ and $\beta_2$ as fitting parameters. The good agreement between theory and experiment can be seen.

### 3.5.2 Experimental Results

In order to confirm that the intrinsic damping of the microcantilever is small compared to beta1 and to quantify it, we performed the ringdown measurement on the system in vacuum ($10^{-5}$ torr). From these measurements it can be seen that the intrinsic damping is much smaller than the damping from the lowest viscosity gas used ($H_2$) with a viscosity of 8.91μPa s. This agrees well with observations made previously [28].

To measure each gas, or binary mixture, the vacuum chamber was filled to atmospheric pressure each gas so measurements could be taken. The values for $\rho$ and $\eta$ for each gas observed, as well as the NIST values (for comparison) can be found in Fig. 3.3. As can be seen, this ringdown method was able to accurately determine both parameters independently. In particular, note that gases with very similar density, but different viscosity ($H_2$ and He) were easily differentiated by the method and the same for similar viscosities and different densities ($CH_4$, $C_2H_6$). In addition, various concentrations of $O_2$ in $N_2$ were measured to show the sensitivity to altered concentrations. Table 3.1 shows density and viscosity of the various mixtures compared to the values predicted by this method. Again, good agreement between the two can be seen.

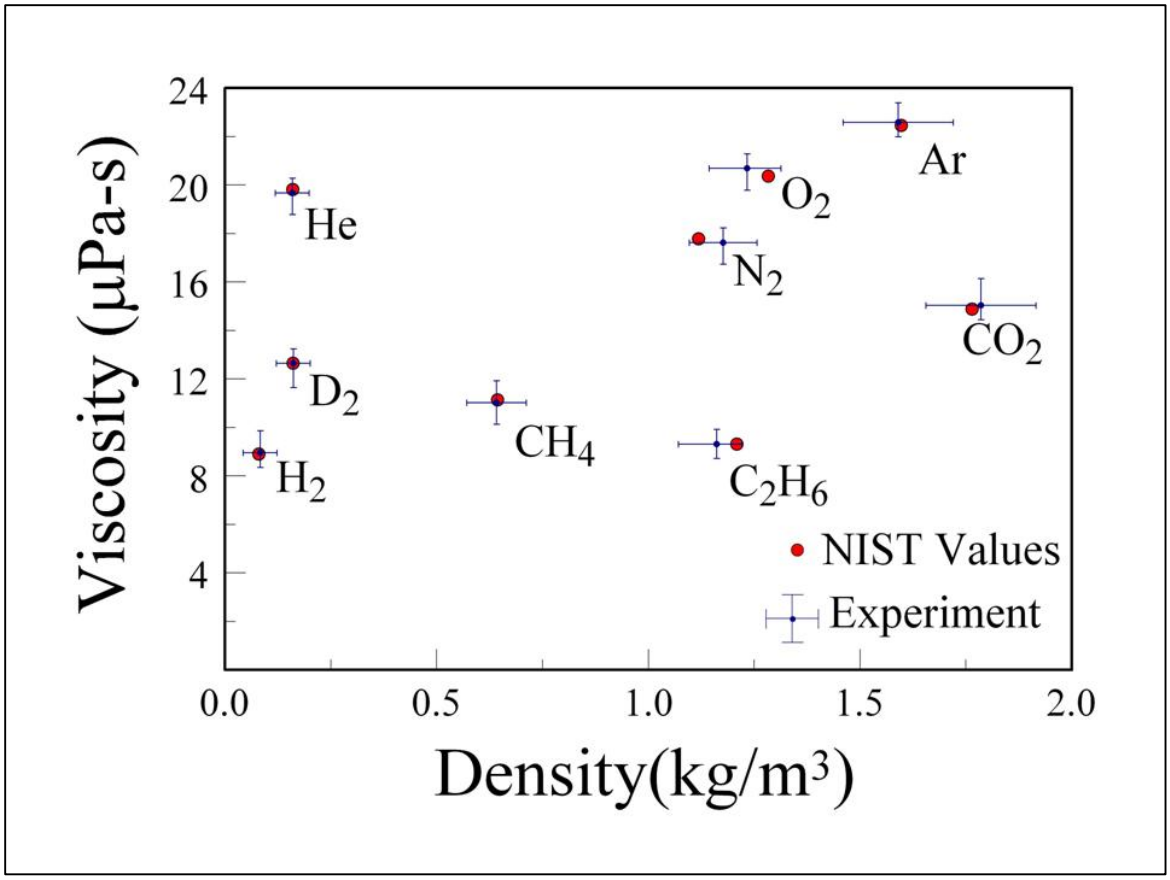


Figure 3.3: (Red dots) Values for the viscosity and density for the gases measured according to NIST standards. (Points with error bars) The values for the same parameters determined by the electrical ring-down method. Gases with similar density, such as $H_2$ and $D_2$, can be easily differentiated with a single measurement using this method as both parameters can be measured simultaneously. Previously, differentiation at this specificity for two different parameters could not be obtained with a single measurement.

Table 3.1: Densities and viscosities of mixtures of $N_2$ and $O_2$ based on both standard values and those observed by the electrical ring-down method. Good agreement with previously reported values and high specificity for the concentration are observed.

| Gas | Density $kg/m^3$ | Predicted Density | Viscosity μPa s | Predicted Viscosity |
|---|---|---|---|---|
| $N_2$ | **1.121** | 1.124 | **17.74** | 17.74 |
| 20%$O_2$ | **1.153** | 1.126 | **18.22** | 18.25 |
| 30%$O_2$ | **1.170** | 1.134 | **18.49** | 18.55 |
| 40%$O_2$ | **1.186** | 1.190 | **18.76** | 18.80 |
| $O_2$ | **1.281** | 1.280 | **20.38** | 20.39 |

# CHAPTER 4

# RESONANCE IN CARBON NANOCOILS

## 4.1 Properties of Carbon Nanocoils

Due to their unique geometry (Fig. 4.1) coiled nanostructures, including silicon and boron carbide nanosprings [31], coiled carbon nanotubes, and carbon nanocoils have been the subject of much study [32]. They have shown many interesting potential applications including as dampeners [33], and as field emitters [34], alone and in composites. In particular, carbon nanosprings have shown promise of altering macroscopic properties when incorporated into mesoscopic systems [33, 35]. In addition, the growth mechanism of these structures (as they self-assemble) has been the subject of much study, owing to the high degree of periodicity they can display [32, 36-38].

Carbon nanosprings generally occur in one of two large categories, coiled carbon nanotubes (cCNT) and carbon nanocoils (CNC). cCNTs have a lattice structure similar to straight carbon nanotubes with pairs of 5,7 defects in the lattice creating the coiled shape. CNCs, by contrast are solid structures approximately homogenous throughout. They are amorphous in structure. The two can be distinguished in an electron microscope as the hollow nature of the cCNTs can be seen. The uses for these objects in NEMS devices are almost limitless as their spring geometry makes them incredibly pliable despite the material strength common to carbon nanostructures.

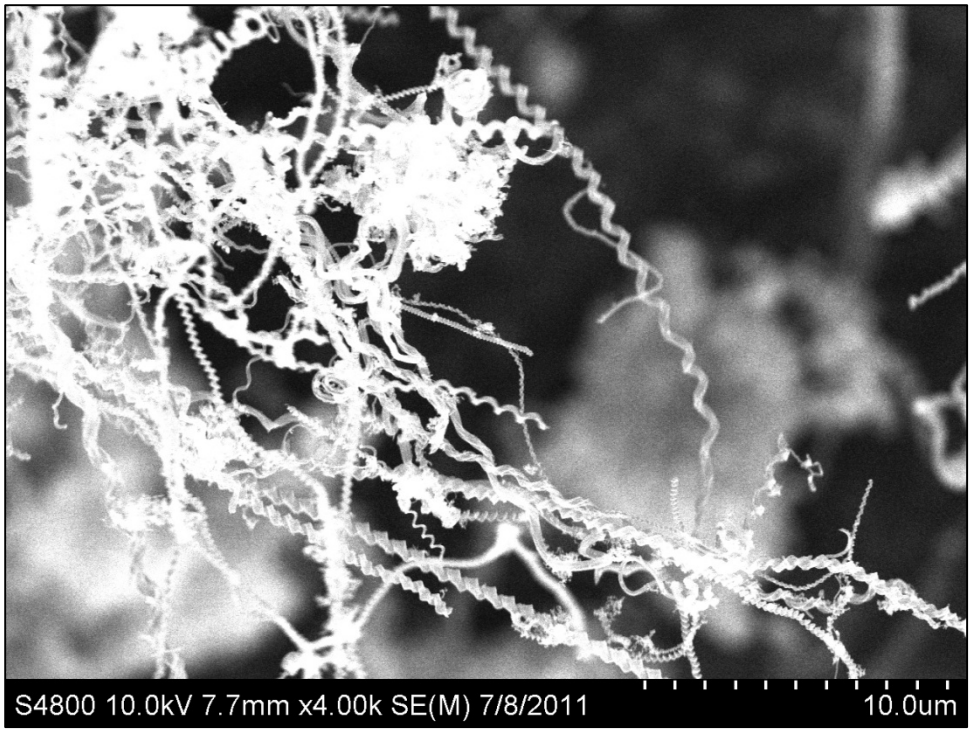


Figure 4.1: SEM image of as prepared cCNW samples

Because the geometry is central to their novelty, their mechanically properties are of particular interest. The information about their resonant behavior which can be obtained from HDR is significantly interesting from this perspective alone. The potential for novel *electrical* properties [39] due to their geometry only enhances the appeal of HDR as a method for exploring these structures. To this end, the resonant behavior of CNCs has been observed using HDR to help determine its material properties [40]. Care was taken to separate the motion from any potential effect from the electron beam.

## 4.2 CNC Synthesis Method

Coiled carbon nanowires were synthesized in a two–stage thermal CVD reactor. The pre-heater and the heater were maintained at $200^0$C and $700^0$C respectively in the presence of Ar (800 sccm). A mixture of xylene and ferrocene was prepared into which tin isopropoxide (source of tin) was added with the ratio of Fe:Sn of 4:1. This precursor was immediately injected into the CVD, using a syringe pump, at the rate of 1 mL/hr. At the same time, 50 sccm of acetylene was passed through the tube at atmospheric pressure. After 2 hr of reaction time, the furnace was shut off along with the acetylene flow for rapid cooling in the presence of Ar. The resultant thick layer of carbon nanocoils grows on a bare quartz substrate.

The growth mechanism for CNCs is still not well understood. In general, it is known that the tube or wire growth is catalyzed, as in straight tube growth, usually by Fe. However, a number of different mechanisms, possibly depending on the synthesis method used and the variety of coils formed, could result in the bending of the structure to form a coil. These include twisting due to asymmetry in the catalyst particle [36] and energy minimization due to In vapors [37].

## 4.3 Experimental Setup and Approach

Because of the small size of the cCNWs compared to the microcantilevers examined earlier, it was necessary to mount the CCE in an SEM, both for vacuum, to increase the amplitude of vibration and thus the electrical signal, and also to observe the motion to confirm resonance while the beam was on. As such, a jig was constructed using

piezoelectric motors (PI Block Nano Positioning System) to alter the geometry and gap distance of the CCE. The jig was then placed in an electron microscope (SU-6600). Ports were designed for the microscope to allow the input and output signals to enter and leave the vacuum chamber. In addition, because of limited space, and electrical pickup, the amplifier had to be redesigned.

In general, pick-up noise in the output wire will be the largest source of noise in our signal after the parasitic signals inherent in the CCE and in the system in general. There are two primary methods of reducing this noise, the first is to shield wires with a common ground, which was done extensively, using coaxial cable whenever possible and adding custom shielding when either space was limited or flexibility in the wire was required. The second method of reducing noise is to reduce the distance from cantilever to amplifier. In order to minimize this distance, our A250 amplifier was modified to accept an external FET, which could then be placed on the jig (see figure 4.2). This was particularly necessary as the nanocantilevers used here were much smaller and thus would hold less charge and output a lower dynamic signal than the microcantilevers used previously.

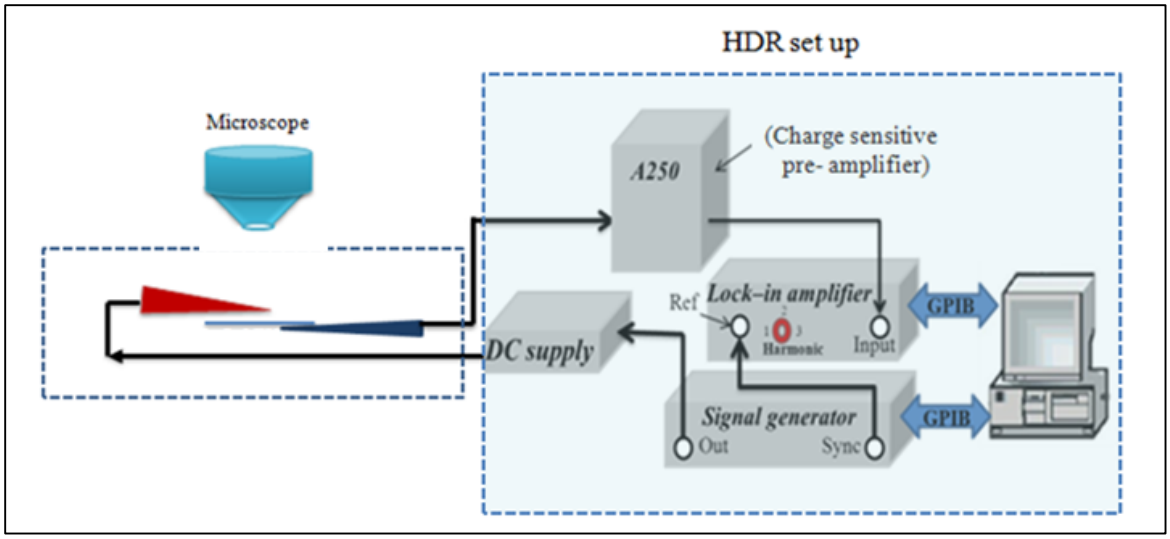


Figure 4.2: Schematic of HDR setup using SU6600 SEM vacuum chamber. The FET is located inside the chamber (left side).

In order to examine the resonance of a cCNW, a small amount of the sample was gathered on a piece of SEM tape and mounted over a darkfield microscope. A sharpened W tip was then used to pull individual coils, held on the tip by Van der Waals forces. This tip was then be mounted in the jig for observation. The cCNW could then be driven to resonance. A detailed description of the electrical configuration can be found in Appendix B.

Because of the small signal to background ratio, it is helpful to perform background subtraction to better analyze the resonant signal. To do this, the ($A$, $\varphi$) polar representation (Chapter 2) is used. A vector from the static cantilever position to the origin in this space is subtracted from the signal (Fig 4.3). This new data can be replotted

as $A$ vs. $\omega$ or $\varphi$ vs. $\omega$ to better visualize the peak. Calculation of peak parameters can be done either with the replotted data, or in the polar representation (See appendix A).

Because of the high pliability of coiled structures, CNCs provide a wonderful opportunity to study nonlinear behavior at large amplitudes. However, to avoid a pull-in instability, the mechanical motion had to be carefully monitored at higher voltages, and the gap distance carefully controlled. While no difference was ever observed in the electrical signal depending on the presence of an electron beam, recorded data was taken with the beam off, to avoid any possible complications from it since electron beam irradiation can significantly affect the electrical properties of nanostructures [41].

In addition to large-amplitude, nonlinear behavior, coils, due to their geometric complexity, are capable of several interesting modes, most more easily accessed than in a straight wire [42-45]. In particular, higher order flexural modes, containing nodal points in their motion, should be more easily observed, as well as axial compression modes.

There are two main issues in the actuation and detection of these more exotic modes. The first are the material constraints on these modes, requiring extremely high frequencies to excite and only creating small amplitudes due to their high energy. Nanocoils naturally overcome most of these due to their flexibility. The second involves the method of actuation. As was discussed in Chapter 2, electrostatic actuation depends on the change in capacitance of the CCE as a function of the deflection or deformation of the cantilever. If the motion of a given mode does not significantly affect the capacitance (compared to say, the change in mechanical energy due to the motion) then the mode will not be sufficiently actuated for any detection scheme, optical or electrical.

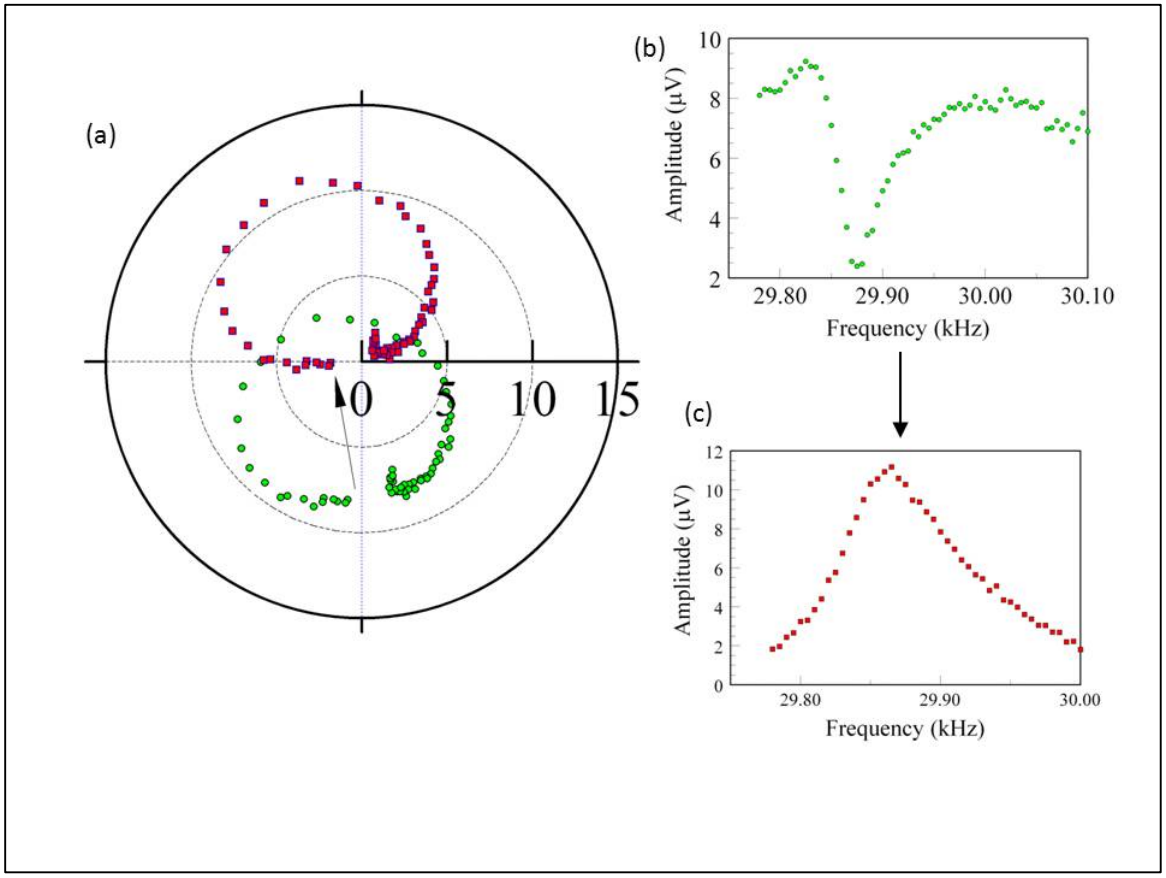


Figure 4.3: (green) Raw data collected for cCNW (a) in the polar representation and (b) as a function of frequency. (red) The same data with a vector added (black line in (a)) to remove background. (c) The resonant peak can be more clearly observed as a function of frequency after this subtraction has been made.

For example, while a nanocoil can be physically driven into a torsional mode much more easily than a wire, the driving force from the counterelectrode on this mode should be very small. As such, even when driving at the natural frequency for this mode, we do not expect significant actuation of it. In addition, if the capacitive change is not large, even for large actuation, the electrical signal will be small (see Eq. 2.4).

In the case of higher order flexural modes, Euler-Bernoulli beam theory gives predictions about the frequencies at which they will occur and they should be relatively easy to actuate, as has been done with other, non-coiled nanostructures [14, 46, 47]. However, because of the nodal points in these higher modes, we expect the electrical signal to be relatively small. While some parts of the cantilever/coil will be moving towards the counterelectrode, increasing the capacitance, others will be simultaneously moving away, decreasing it. As a result, though we may expect to observe the mode physically, detecting it electrically should be considerably more difficult.

## 4.4 Experimental Results

For the coil examined (material parameters are given in Table 4.1) the resonance of the first mode was observed, simultaneously using the SEM and HDR, at driving frequencies of 14.9 and 29.8 kHz. As before, comparing the two (the amplitude of vibration for the coil and the output of the amplifier) shows that they closely match (Fig. 4.4), verifying both the source of the electrical signal and the reliability with which it represents the physical motion. The presence of amplitude at both frequencies is expected since, as discussed extensively in Chapter 2, the cantilever will effectively be driven at

both $\omega$ and 2 $\omega$. The second mode of oscillation was also observed at a driving frequency of 190 kHz. However, for the reasons mentioned above, no electrical signal could be observed, only the physical motion (Fig. 4.4.2). For similar reasons, no motion was seen at 95 kHz (where the 2 $\omega$ frequency should give rise to a peak). In this case, the normally smaller amplitude actuated when driven at half the resonant frequency (see Fig 2.3.3) is the biggest factor.

We note the ratio of the second mode of vibration to the first is 190 kHz/29.8 kHz = 6.375. For the ideal Euler-Bernoulli beam, this ratio should be 6.267. This small discrepancy shows both that the motion of the nanocoil is not exactly that of a free cantilever (due both to its geometry and to the complicated driving force) and that the second mode is indeed at 190 kHZ as opposed to 380 (driven by the 2$\omega$ term).

Additionally, at larger amplitudes of vibration (due to higher driving voltage and smaller gap distance for the CCE), the characteristic nonlinear Duffing behavior was observed (Fig. 4.6). Because of the softness of the coil (as opposed to more rigid geometries) higher amplitudes could be more easily obtained and more extreme Duffing behavior could be observed, such as the hysteresis depending on the direction of scanning seen in Figure 4.6. Beyond this, when the nonlinearity of the restoring force was increased further (for extremely small gap distances) two new resonances were observed with different polarizations from those observed at lower amplitudes. At a frequency near the linear resonance, a combination mode was observed, with both an axial and lateral component. At the maximum amplitude for this mode the change in length as the coil resonates can be clearly observed (Fig. 4.7). This peak was asymmetric, although no

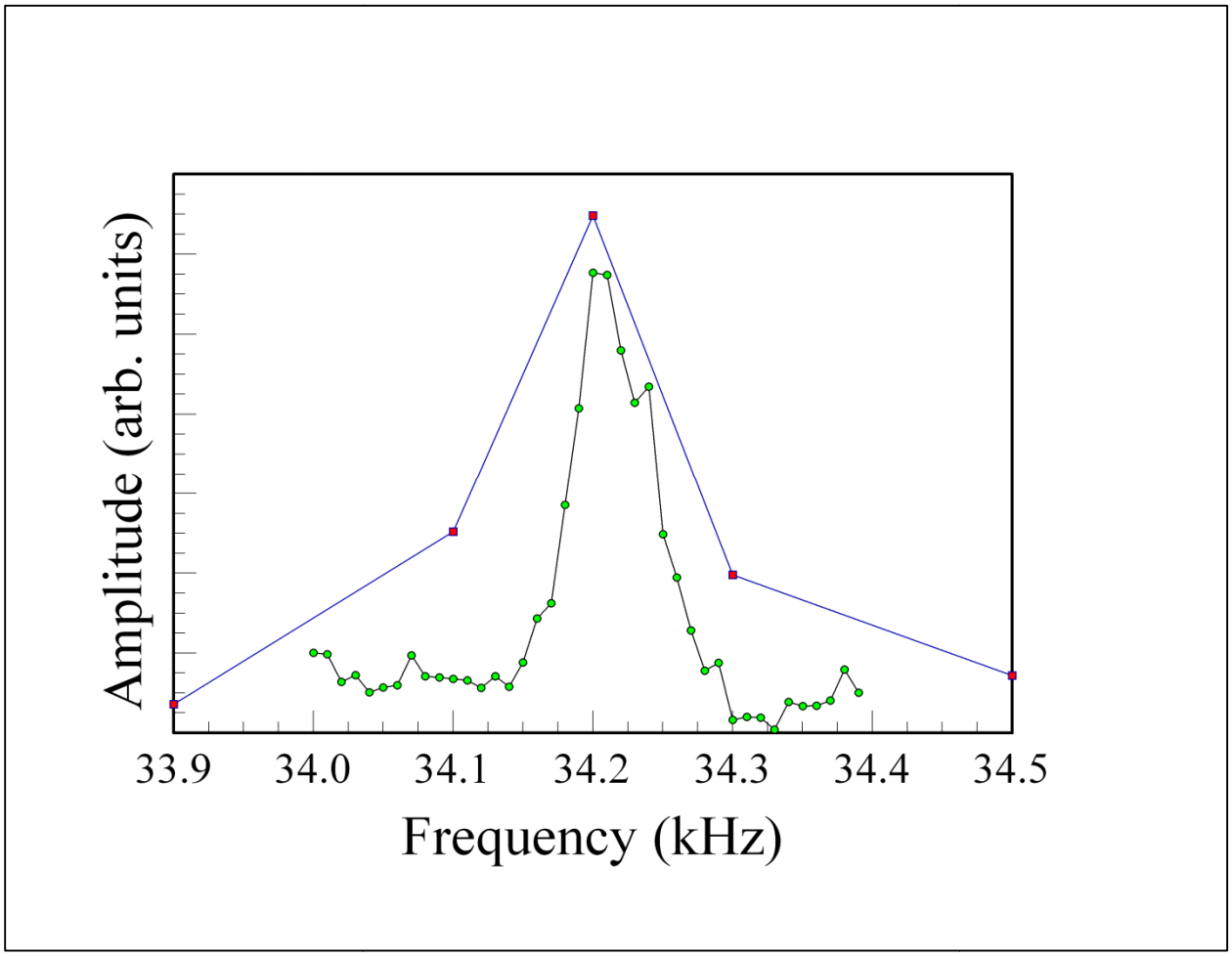


Figure 4.4: The visual amplitude is shown by the red squares and the electrical amplitude by the green circles. As can be seen, the electrical peak closely matches the observed mechanical resonance, showing that the electrical signal does represent the mechanical motion.

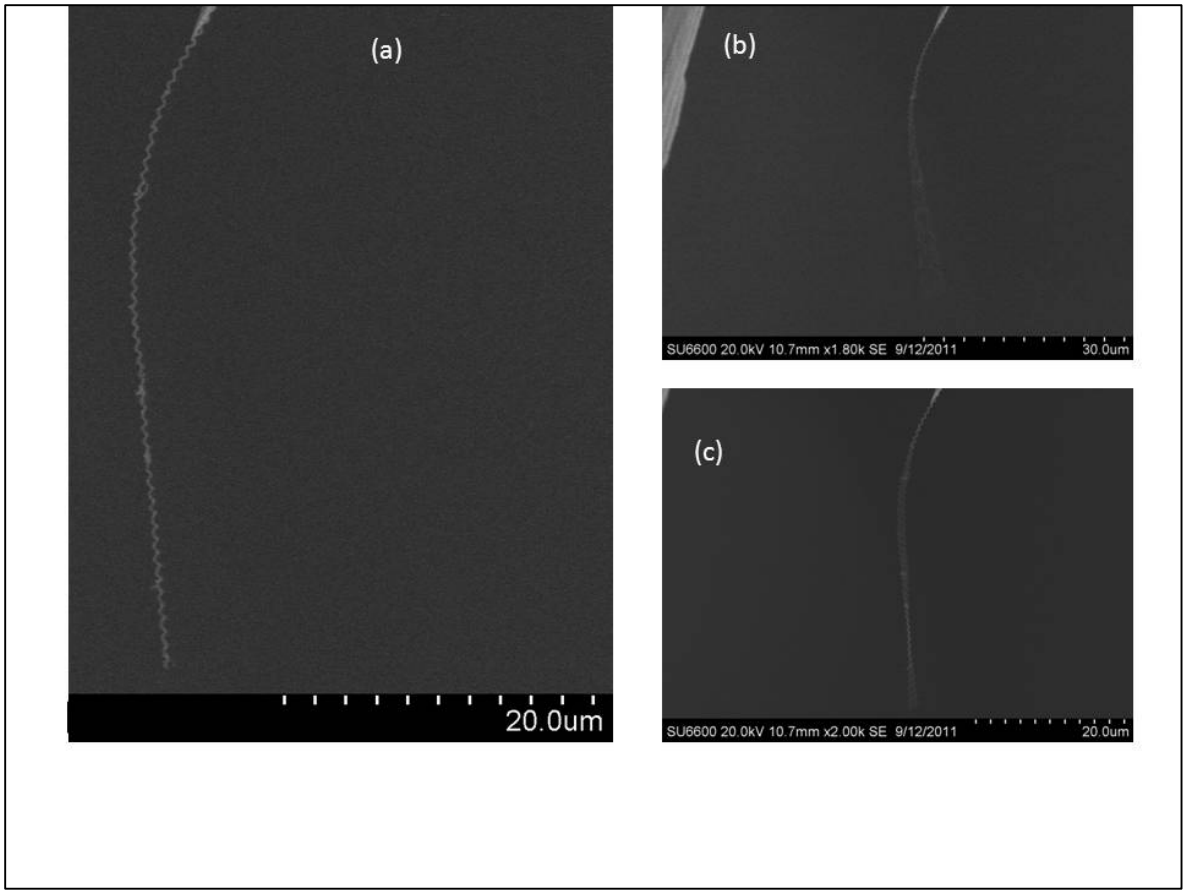


Figure 4.5: SEM image of the cCNW driven (a) away from resonance, (b) at its first mode (~30 kHz) and (c) at its second mode (~190 kHz). The counterelectrode can be seen in the upper corner of (b), and the different mode shapes can be clearly observed between (b) and (c).

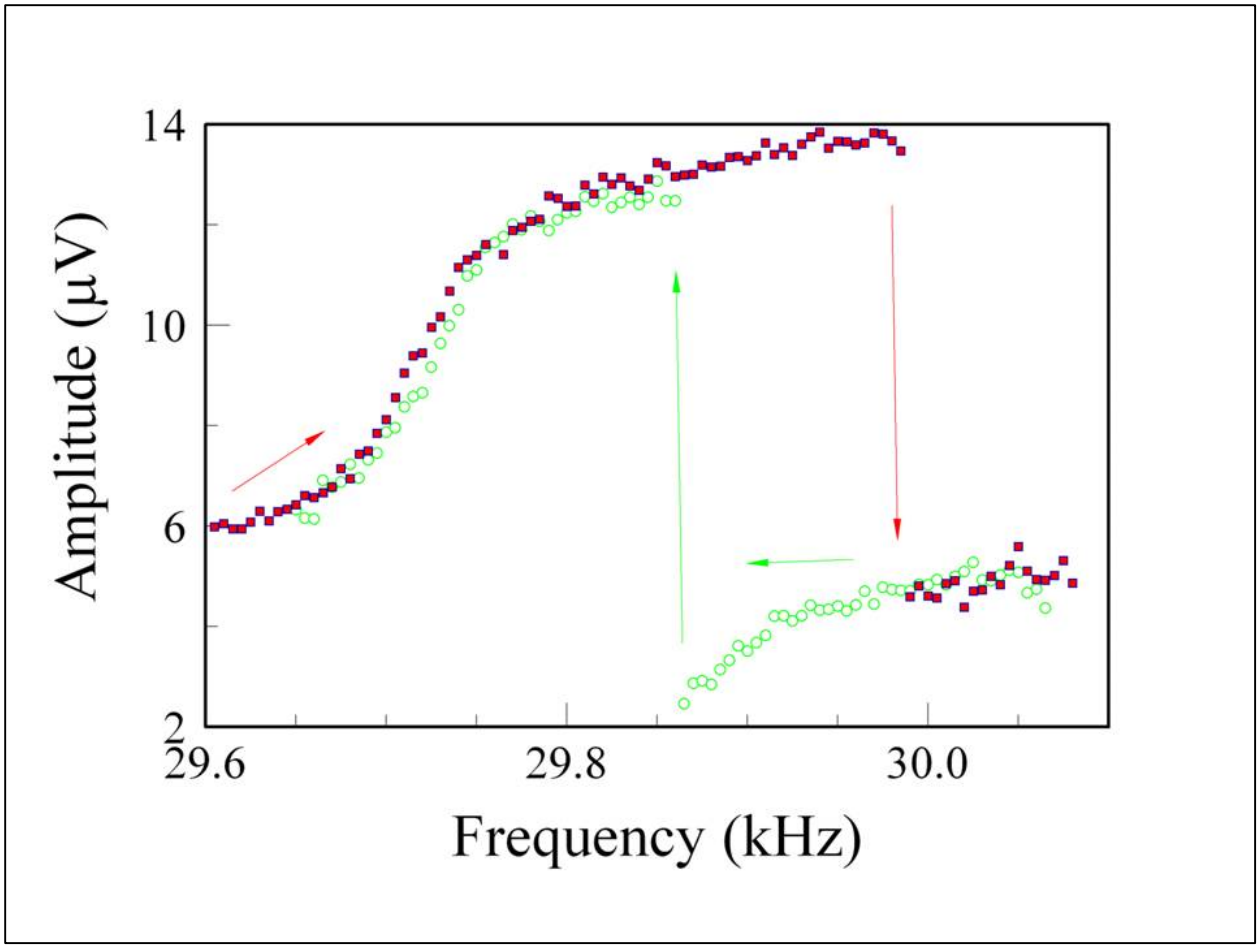


Figure 4.6: Electrical output from the cCNW resonance at a driving voltage of 6V. The red points were for increasing frequency, the green for decreasing. The super-critical Duffing behavior and hysteretic effects can be clearly seen.

hysteresis was observed. At a slightly higher frequency, the other nonlinear mode observed appears to be circularly polarized as opposed to the normal linear polarization observed for all samples previously (Fig. 4.8). Clear hysteresis could be seen in this peak (Fig. 4.9). Interesting, while electrical signals could be seen for both peaks, the linear peak showed a much greater amplitude than the circularly polarized one. This is probably

Table 4.1: Parameters of the cCNW observed to determine its material parameters

| $\rho$ | $N$ | $r$ | $R$ | $L$ |
|---|---|---|---|---|
| 2 g/cm$^3$ | 52 | 400 nm | 800 nm | 42 μm |

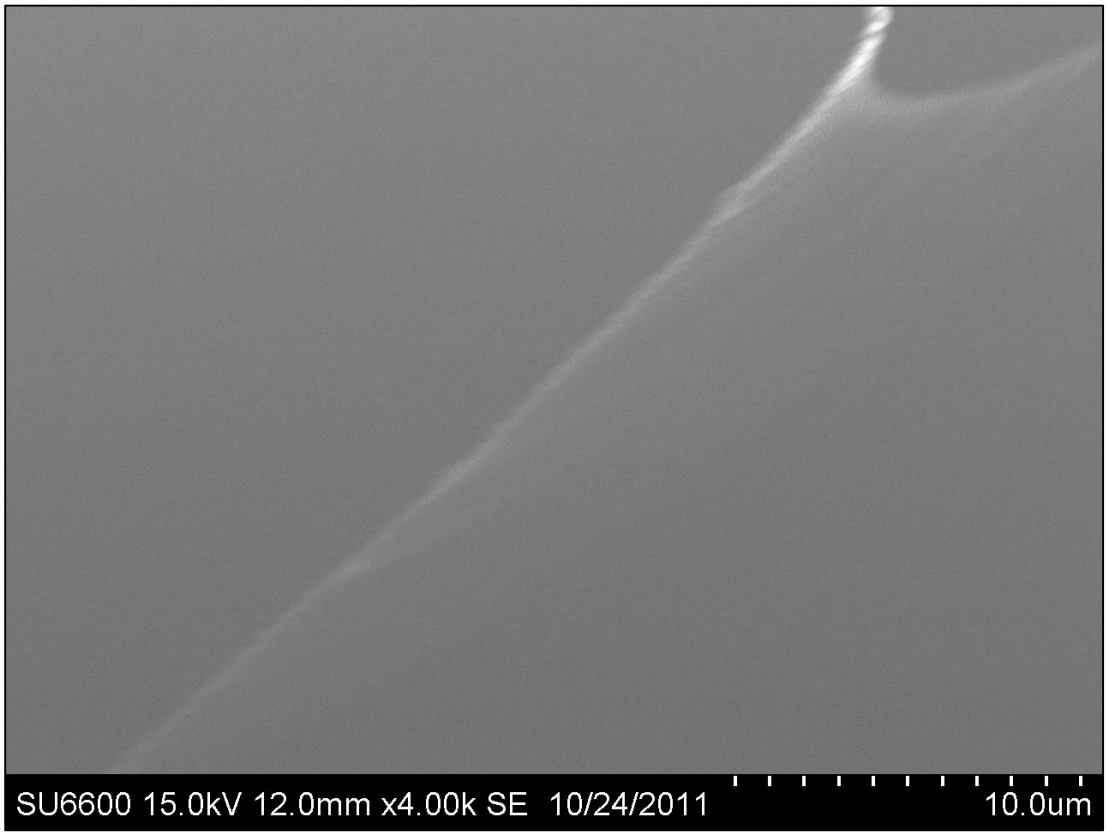


Figure 4.7: SEM image of the combination mode. The stretching and compression of the cCNW can be seen on the left and right sides of the motion respectively.

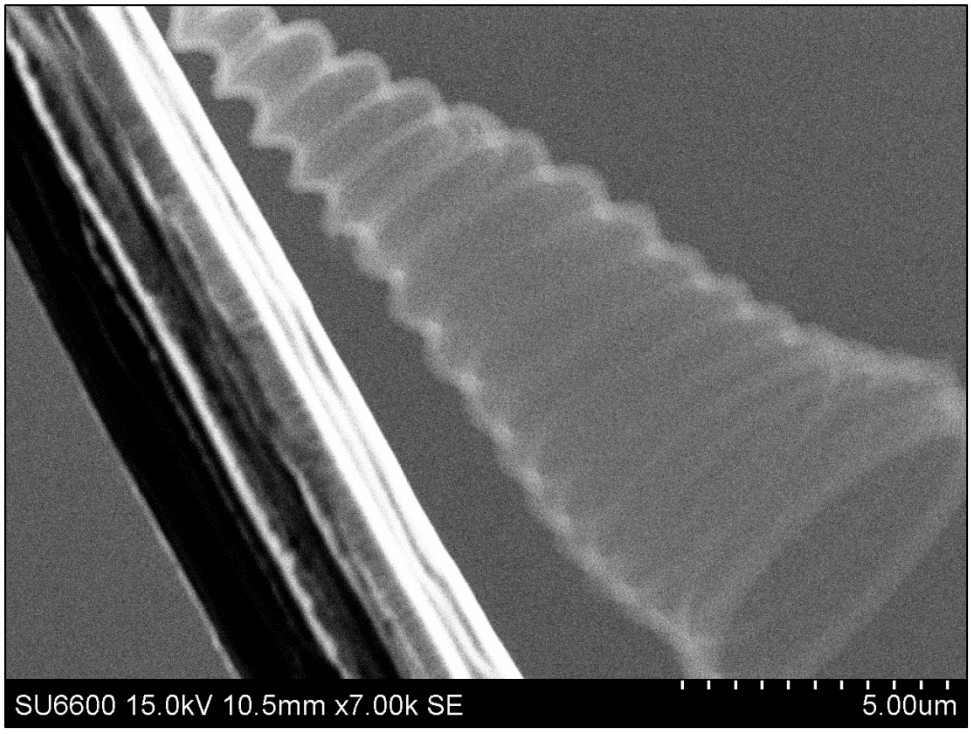


Figure 4.8: SEM image of the circularly polarized mode. The counterelectrode is pictured on the left.

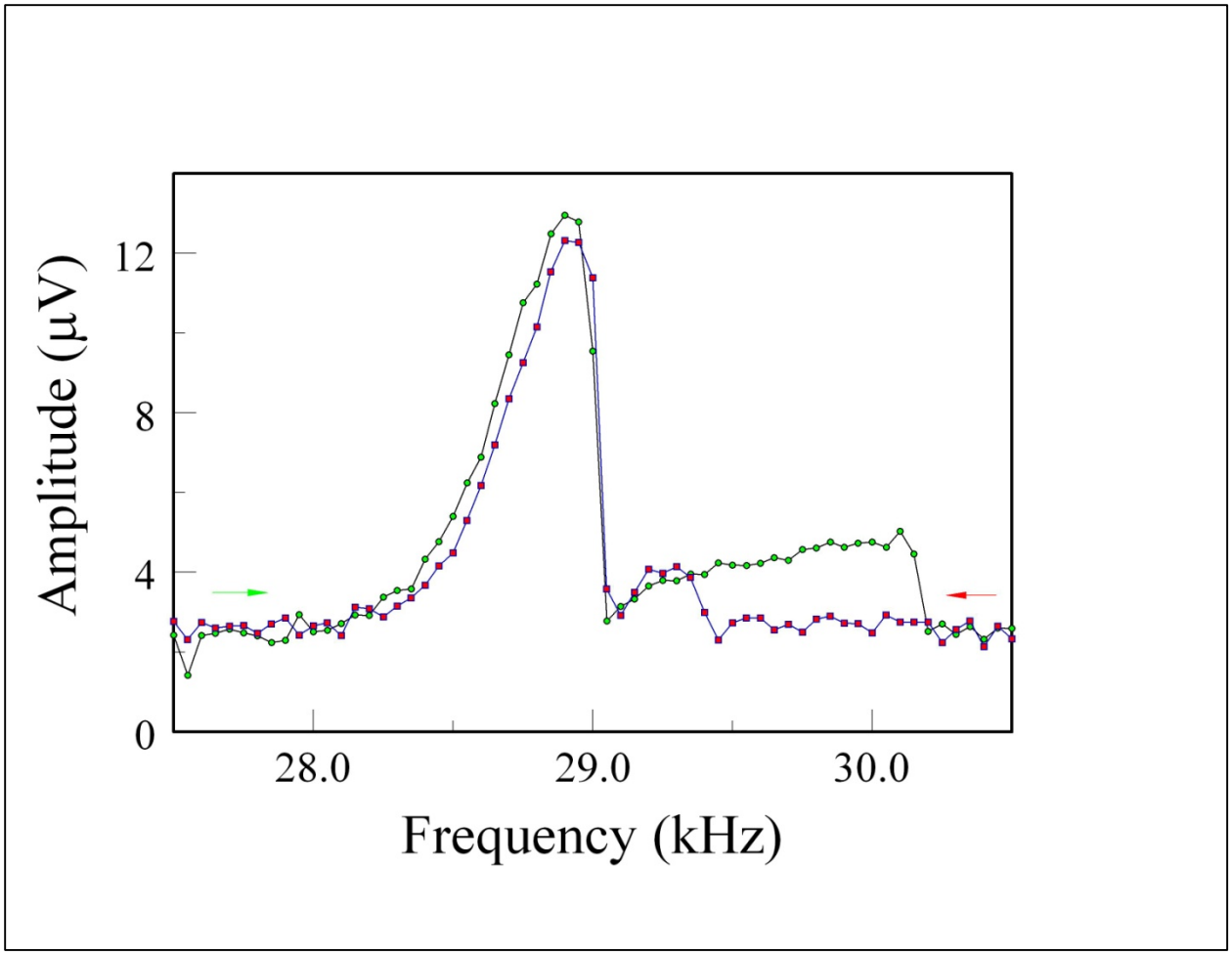


Figure 4.9: Electrical signal in the (green) increasing and (red) decreasing frequency directions for the combination and circularly polarized resonances. The large, lower frequency peak is due to the combination mode. The asymmetry of this mode can be clearly seen, although there is no hysteresis. The small, high frequency mode is due to the circular polarization. Significant hysteresis can be seen between the forward and back directions.

due to the relative change in capacitance caused by the two different motions as mentioned above.

## 4.5 Discussion

From the above experimental results we will focus on a pair of useful results, both of which emphasize the usefulness and applicability of the HDR method. For the first, we will use the resonant frequency, which can be precisely determined from the electrical output to determine the lateral spring constant of the CNC, which could, in principle, be using to further investigate its material properties. For the second, we will examine the unique nonlinear behavior we observed to investigate this larger nonlinear regime and our ability to explore it.

### 4.5.1 Linear Results: Determination of the Lateral Spring Constant

Using the resonant frequency of the first mode (or in principle of any mode) we can calculate the lateral spring constant of the nanocoil, as has been done previously with carbon nanotubes [48]. We can write the Euler-Bernoulli beam equation with appropriate fixed free boundary conditions for the coil:

$$EI\frac{\partial^4 y(x,t)}{\partial x^4} = \rho A\frac{\partial^2 y(x,t)}{\partial t^2} \tag{4.1}$$

$$y(0,t) = 0 \tag{4.2}$$

$$y'(0,t) = 0 \tag{4.3}$$

$$y''(L,t) = 0 \tag{4.4}$$

$$y'''(L,t) = 0 \tag{4.5}$$

where $E$ is the Young's modulus of the beam, $I$ is its moment of area, $\rho$ is the density, $A$ is the cross sectional area, $x$ is the position along the beam, $t$ is time, and $y$ is the deflection of the beam a distance, $x$, from the held end at time, $t$. Primes denote differentiation with respect to $x$. We assume here that the CNC can be approximated as a thin wire. This equation can be solved for the natural frequencies of vibration (assuming, for now, a simple narrow wire):

$$f_{1,2} = \left(\frac{n_{1,2}^2}{2\pi}\right)\sqrt{\frac{k}{0.23m}} \tag{4.6}$$

where f is the frequency of the mode, m is the mass of the beam, and $k=EI/L^3$ is the compliance, or lateral spring constant. The number $n_k$, is the solution to the transcendental equation:

$$\cos n_k \cosh n_k = -1 \tag{4.7}$$

derived from the Euler-Bernoulli equation where k is the number of the mode in question. The first two of these values are $n_1 \approx 1.875$ and $n_2 \approx 4.694$. Theoretical models have approximated the effective mass of a fixed free cantilever (necessary because the motion of any point on the cantilever is dependent on the distance from the base) as 0.23 m, where m is the actual mass. We can approximate the mass of our coil using:

$$m = 2\pi^2 \rho r^2 N \sqrt{R^2 + \left({}^{L}/_{2N\pi}\right)^2} \tag{4.8}$$

where *r* is the small radius of the wire comprising the coil, *R* is the radius of the coil itself, and *N* is the number of coils. The equation can be derived in a straight forward manner by calculating the total arc length of the CNC and assuming a circularly cross section and uniform density along this length. Plugging in our values from Table 4.1, the mass is calculated to be 260 picograms, for an effective mass of 61 picograms. Plugging

into Eq. 4.5 along with the natural frequency of the first mode (29.8 kHz), we find the lateral spring constant to be 176 uN/m.

For a simpler geometry, we could use this information to determine the material parameters of the CNC, namely the Young's modulus. Much work has been done analyzing the motion of coiled cantilevers [40, 44, 45]. However, even using very general approximations, the equations relating both the Young's modulus and the sheer modulus are complicated and hopelessly entangled. Sato et al. [49], give the following equation for the spring constant, using only the sheer modulus as a free parameter:

$$k = {3G_0 r^4 (R^2 + (R - 2r)^2)}/{16R^3 L^2 N} \tag{4.9}$$

where $G_0$ is the sheer modulus. Using our lateral spring constant, we can derive a value for the sheer modulus of 2.7 GPa similar to what has been observed in other carbon structures. However, this equation, using only a sheer modulus, assumes only sheer motion in the CNC, accurate only for a very small pitch and long length compared to the radius of both the coil and the wire and the deflection respectively.

### 4.5.2 Nonlinear behavior

Perisanu et al. [50] have previously observed a circularly polarized mode in MWNTs and SiC nanowires. The behavior they observe is similar to that seen in the CNC, including the relative spring softening for the CP and the spring hardening for the

Duffing behavior. They explain this mode using a coupling between the two linear polarizations, which should be nearly identical (ignoring the direction of actuation) for an isotropic wire or coil. The only coupling required by their method, and the source of their nonlinear terms, is the constraint that the length of their nanotube or nanowire be constant. This gives rise directly to a resonance near the linear resonant frequency, but always with a hard-spring behavior.

The situation is similar for our CNC sample. For large enough amplitude motion, it becomes more favorable for the nanocoil to move in a circular motion, keeping its length relatively constant, than to deform and remain linearly polarized. The CP mode, however, because of its motion out of the CCE plain, does not effect nearly the same change in capacitance as the linear polarization in the Duffing regime or otherwise. In addition, depending on the exact shape of the modes, the Duffing regime can display either a hard or soft spring behavior. Under certain excitations (depending on gap distance, driving voltage and the individual coil), Duffing behavior could be observed deviating from the natural frequency of the cantilever in the same direction (higher frequency) as the circularly polarized mode.

We can even see, in the combination mode, that it experiences spring hardening, evident from the asymmetry of the resonant peak. However, as can be seen in Fig. 4.9, the two peaks occupy separate regions in the frequency spectrum. The combination peak indicates that observation of a purely axial mode for some cCNWs is indeed possible and should give rise to a detectable electrical response. By simply changing the relative angle between the coil and the gap with the counterelectrode, the combination response can

contain more or less of the lateral and axial components respectively, with the response being almost entirely lateral in the normal configuration and entirely axial in an end-on configuration with the coil pointing towards the counterelectrode. If a fully axial mode can be observed, more accurate calculations can be made on the material parameters of the cCNW, as this geometrically simple motion allows for easier computation of the sheer modulus.

# CHAPTER 5

# INTRINSIC DAMPING IN A MWNT

## 5.1 Multi-Walled Carbon Nanotubes

Multi-walled carbon nanotubes (MWNTs) present one of the most interesting and versatile areas of development in nanotechnology. Thanks continuing innovation in their synthesis , MWNTs can now be produced on industrial scales at a reasonable cost. Recent work has been done functionalizing MWNTs for use in nanocomposites [51, 52], chemistry [53, 54], and even medicine [55-57].Interestingly, technology has recently been developed to produce spinnable MWNTs from ultra-long, aligned samples. These may be pulled from their substrate and spun and woven into threads [58], with a variety of material uses.

In addition, MWNTs are an interesting opportunity to test low dimensional physics. As they are essentially graphite sheets, curled into a tube, they display a number of interesting mechanical and electrical properties that can be modeled and explained with simple theoretical considerations, although the complicated interaction among layers of the nanotube introduce computational difficulties over single-walled carbon nanotubes (SWNTs). They are known to be conducting [59, 60], even though SWNTs can be either metallic or semi-conducting, depending on the chirality. This is due to interaction between layers. MWNTs are also very strong, having a theoretical Young's modulus of 1 TPa or higher, with experiments giving similarly large results [61-63]. This extremely high strength opens up amazing possibilities for nanotube based materials and devices.

As noted above, the interaction among layers in a MWNT is particularly interesting, as it complicates both the electrical and mechanical properties of the tube. Of particular interest is the dissipation mechanisms caused by this interaction and others in the nanotube. By observing the intrinsic damping in a resonating MWNT, we can obtain information regarding the source of this damping. As the quality factor of a resonator is a significant factor in its practicality as a device component, understanding these mechanisms is an important step towards implementing MWNT based technology.

## 5.2 Sources of Damping in a Resonating MWNT

If a MWNT (or any real structure) is driven to resonance, dissipative mechanisms will convert the mechanical energy into other forms. This dissipation will increase $\gamma$ (from Eq. 2.11):

$$\frac{d^2x}{dt^2} + 2\gamma\frac{dx}{dt} + \omega_0^2 x = \frac{F_c}{m} \tag{5.1}$$

which will in turn will increase the observed damping and decrease the quality factor, $Q$, of the resonator:

$$Q = {\omega_0}/{2\gamma} \tag{5.2}$$

where $\gamma$ is the damping of the cantilever as defined in Chapter 2. We differentiate here between external damping, such as from a gaseous environment (see Chapter 3) and intrinsic damping due to mechanisms in the cantilever itself. There are several mechanisms for intrinsic damping in a MWNT which are suspected to affect the resonant motion, including telescoping motion, (5,7) defects, interaction with phonons, and poor junction contact.

Modeling has been done related to the telescoping motion of layers in a MWNT [64]. This is essentially the sliding of layers against each other and it will be a significant source of dissipation in a MWNT if actuated. It will also cause a change in the total length of the nanotube (hence, telescoping). Because the layers of a MWNT are relatively loosely bound, motion of this type should be easily actuated.

As a MWNT bends in response to an external force (for example electrostatic driving), it has been shown that pairs of (5,7) defects (so named because of the pentagon and heptagon shapes which appear in the deformed lattice) can be an energetically favorable transition to accommodate the stress on the nanotube [65]. In a resonating MWNT, a number of these defects would be constantly forming and relaxing to minimize the energy of the MWNT lattice. The rate at which the lattice can create and eliminate these defects will be critical to their appearance in a resonating MWNT.

Inherent in any real material, phonon creation will be a mechanism for dissipation. The mechanical energy of resonance will be converted into phonons in the lattice which can then propagate through the lattice, increasing its temperature. This dissipation will be unavoidable, but can be reduced by working at a low temperature. It

should also occur even for extremely small amplitudes of vibration, as opposed to some other dissipation mechanisms (see below). In addition, heat flow due to the thermal gradient across the cantilever will cause the dissipation of energy as the compressed side of the coil and the elongated side of the coil exchange energy.

Finally, the junction between the MWNT and the W tip can be a source of dissipation. Ideally, the MWNT should be rigidly connected so the boundary conditions for a cantilever (Eq. 4.2, 4.3) are maintained. However, if the nanotube can slip slightly at this point, friction will produce heat and damp the motion of the cantilever. In addition, if the contact is too weak, resistance between the MWNT and W tip may prevent an electrical output from being observed. In order to reduce this possibility, an electrical current was supplied through the MWNT. Because of its small diameter, the large amount of heat produced by this current effectively welded the nanotubes to the tip. As will be discussed below, however, it is evident the contact is still a significant source of dissipation.

It is important to note that the advent of these mechanisms in the motion of the MWNT is, in several cases, dependent on a critical deflection being reached. For the telescoping motion, the pull on an inner layer must be enough for it to slide one site further along the layer containing it. Below this critical force, the layers will not slide against one another and no dissipation will occur through this mechanism. Similarly, below a critical deflection, the creation of defects in the MWNT will not be favorable and the lattice will remain unchanged. At finite temperatures, particularly at room

temperature under which the HDR experiments have been performed, phonon creation should occur essentially continuously for any detectable deflection.

Because telescoping motion and defect creation should occur discretely as a function of deflection, we can expect the measured intrinsic damping in the MWNT should vary depending on the amplitude of vibration. Ideally, the onset of a new dissipation mechanism should create discrete changes in the quality factor of the resonator, which could then be observed. However, because of the large number of layers in a typical MWNT, the number of dissipation mechanisms is large and a continuously changing quality factor as a function of amplitude of vibration is expected. The goal, therefore, is the observation of this essentially nonlinear damping ($\gamma=\gamma(x)$). Similar observations of an amplitude dependent quality factor have been made for a doubly clamped nanotube at ultra-low temperatures [66].

## 5.3 Synthesis

Long MWNTs were synthesized in a two–stage thermal CVD reactor. The pre-heater and the heater were maintained at $250^0$C and $850^0$C respectively in the presence of Ar (200 sccm). A mixture of xylene (10 mL) and ferrocene (400 mg) was prepared. This precursor was immediately injected into the CVD, using a syringe pump, at the rate of 9 mL/hr. At the same time, 240 sccm $H_2$ and 1.5 sccm $O_2$ was passed through the tube. After 1 hr of reaction time, the furnace was shut off along with the reactive gas flow for rapid cooling in the presence of Ar. The resultant thick layer of MWNTs grows on a bare quartz substrate.

## 5.4 Experimental Results

A MWNT was mounted and placed in the SU6600 exactly as described for the CNC (chapter 4). Mechanical resonance was observed at a frequency around 84 kHz (Fig. 5.1). However, poor contact with the W tip caused the resonant frequency to drift while the nanotube was in motion. Over time, the resonant frequency would decrease as measurements were taken. Mostly likely the motion of the MWNT was separating it from the W tip, increasing the effective length and decreasing the resonant frequency. If the MWNT was allowed to sit without resonating for a long period of time, the frequency would gradually increase back to its original value as electrostatic forces reattached it to the tip. Ion beam deposition could not be effectively used for the MWNT, as it was for the nanocoil, due to the smaller size of the MWNT. The effective spot size of deposition for the ion beam system available was large enough to coat the entire MWNT (partially through capillary action) as opposed to just the base where it was connected.

Regardless, the shape of the resonant peak did not vary with repeated trials, only the frequency (Fig. 5.2). In order to measure the effects of nonlinear damping, resonant spectra were taken for the MWNT for several values of the driving voltage, ranging from 3 to 8 V. Background subtraction could be performed (as in Chapter 4) to more easily visualize the peak. In order to calculate the quality factor, the polar representations of the resonant peaks were used. As discussed previously (Chapter 2), in polar coordinates ($A$, $\varphi$), a normal resonant peak should form a circle. If we bisect the circle with a line connecting the maximum amplitude and a point out of resonance, a line bisecting this

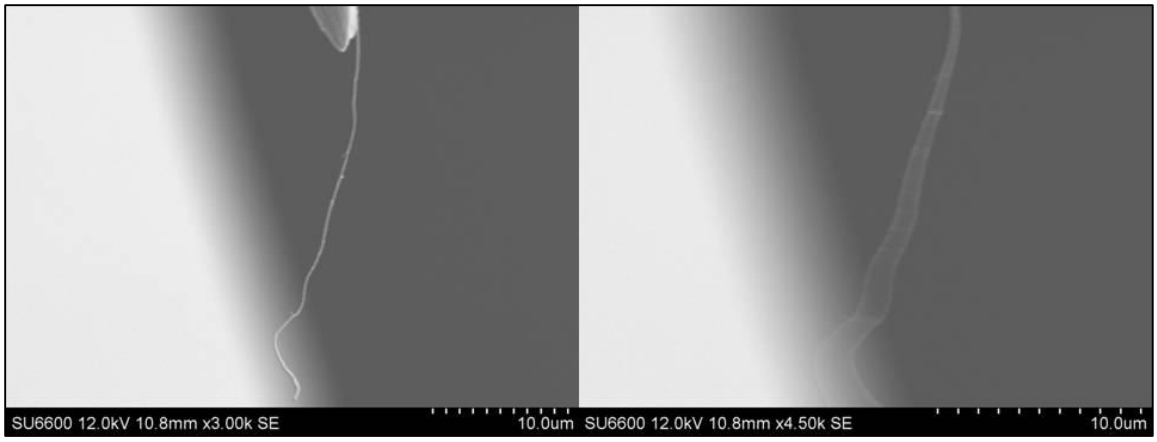


Figure 5.1: SEM image of MWNT in close proximity to the W counterelectrode (left) out of resonance and (right) resonating at its first mode.

will connect 2 points which can be used for the full-width at half maximum (See appendix A). By using this method, we are able to accurately calculate a quality factor even in the presence of a background and even in the Duffing regime.

## 5.5 Discussion

As can be seen (Figs. 5.3, 5.4), the quality factor does undergo a change as the amplitude increases. While the uncertainty in the measurement of quality factor makes it difficult to determine the nature of this change, it does not occur linearly as a function of amplitude, with a few regions where the quality factors changes rapidly between values of the driving voltage. As discussed above, this is possibly due to exceeding critical amplitudes where new defects can affect the resonant motion. Duffing behavior was also observed, as before, with critical Duffing behavior and the resulting hysteresis occurring at driving voltages over 6 V. While the onset of this behavior should not change the

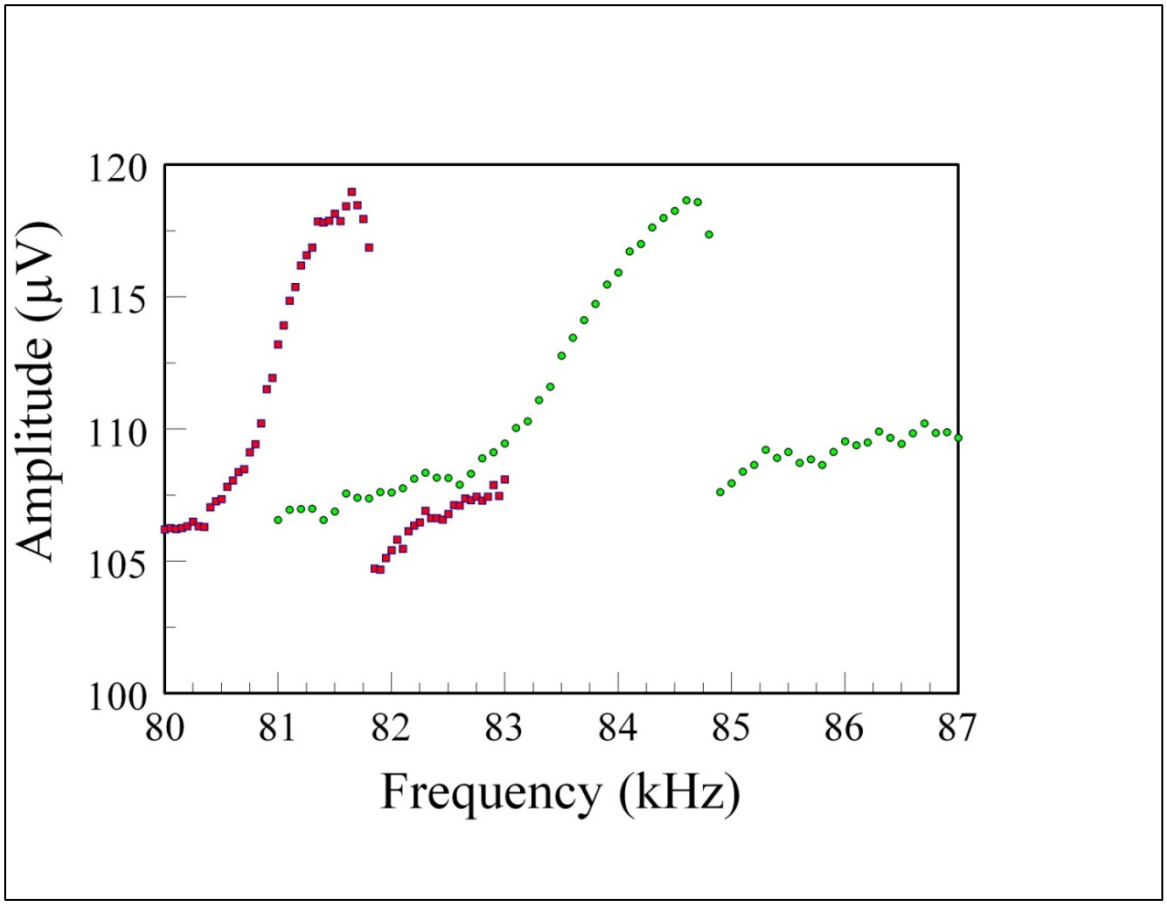


Figure 5.2: Electrical output of resonating MWNT for the same driving voltage (8V) taken an hour apart. The frequency can clearly be seen to drift. The shape of the peak, however, remains relatively constant.

observed damping, it does complicate the calculation of the quality factor for these curves as the unstable region of the solution to the Duffing equation cannot be directly observed. This is alleviated by the using polar representations to calculate Q, but the shift in the maximum frequency (spring hardening in this case) does increase the uncertainty of the calculation for larger driving voltages.

From the decrease in quality factor as a function of amplitude, we can conclude that nonlinear damping plays a significant role in the resonant behavior of MWNTs. Once the precision of this technique increases, and SWNTs can be effectively studied, it is reasonable to expect observation of clearly delineated discrete changes in quality factor as a function of amplitude due to the onset of individual defects. For larger, more complicated MWNTs, the large number of these defects, as well as large dissipation at the nanotube/W tip junction, blur these steps into a continuum. Surprisingly, there still do appear to be regions of rapid change versus amplitude, probably due to the onset of a large number of defects around critical amplitudes (i.e. where the Euler-Bernoulli beam equation begins to break down or the onset of Duffing behavior).

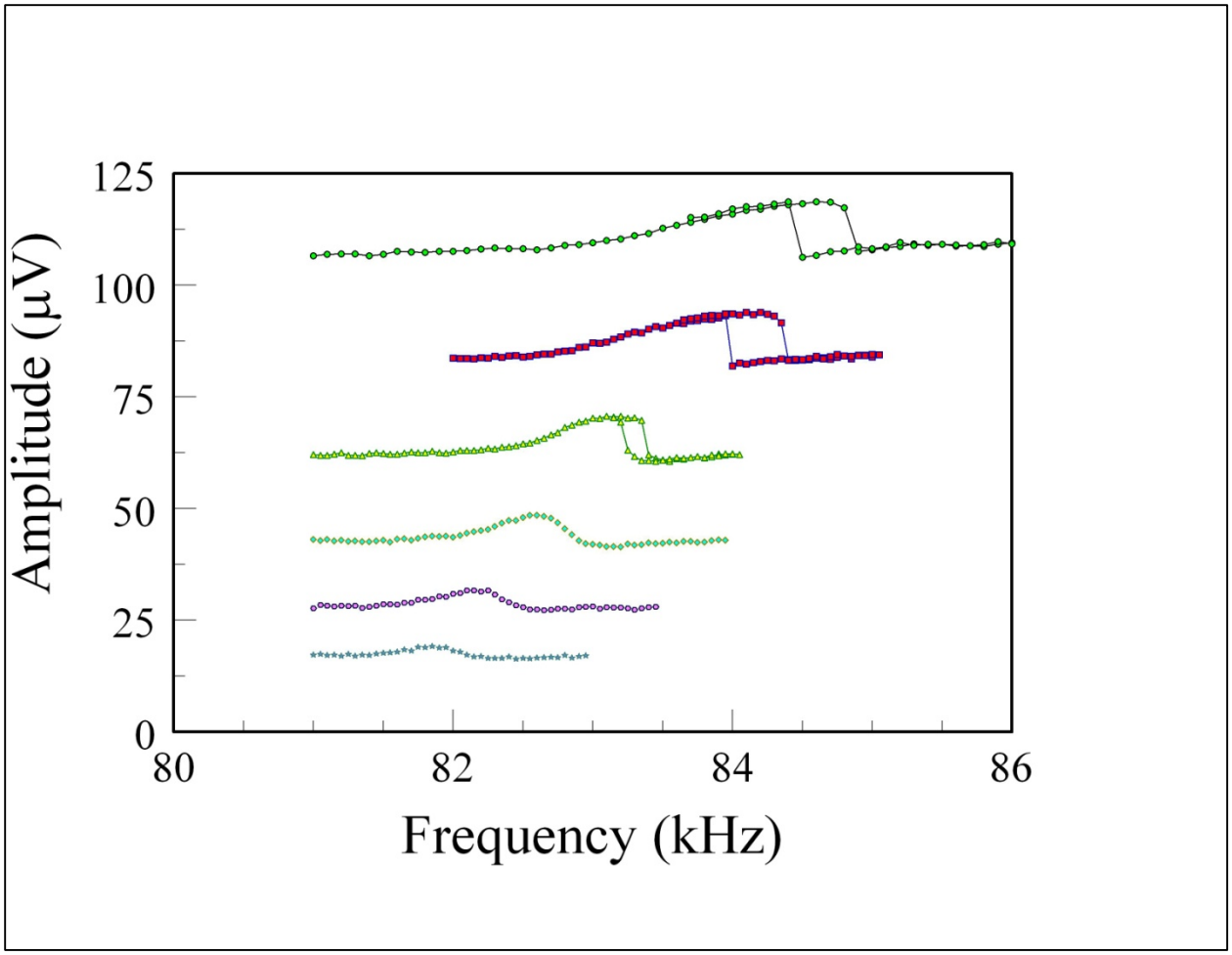


Figure 5.3: Electrical output from the resonating MWNT for a driving voltage of 3V (bottom curve) increasing by 1V up to 8V (top curve). Hysteresis can be observed for 6V, 7V, and 8V driving voltage.

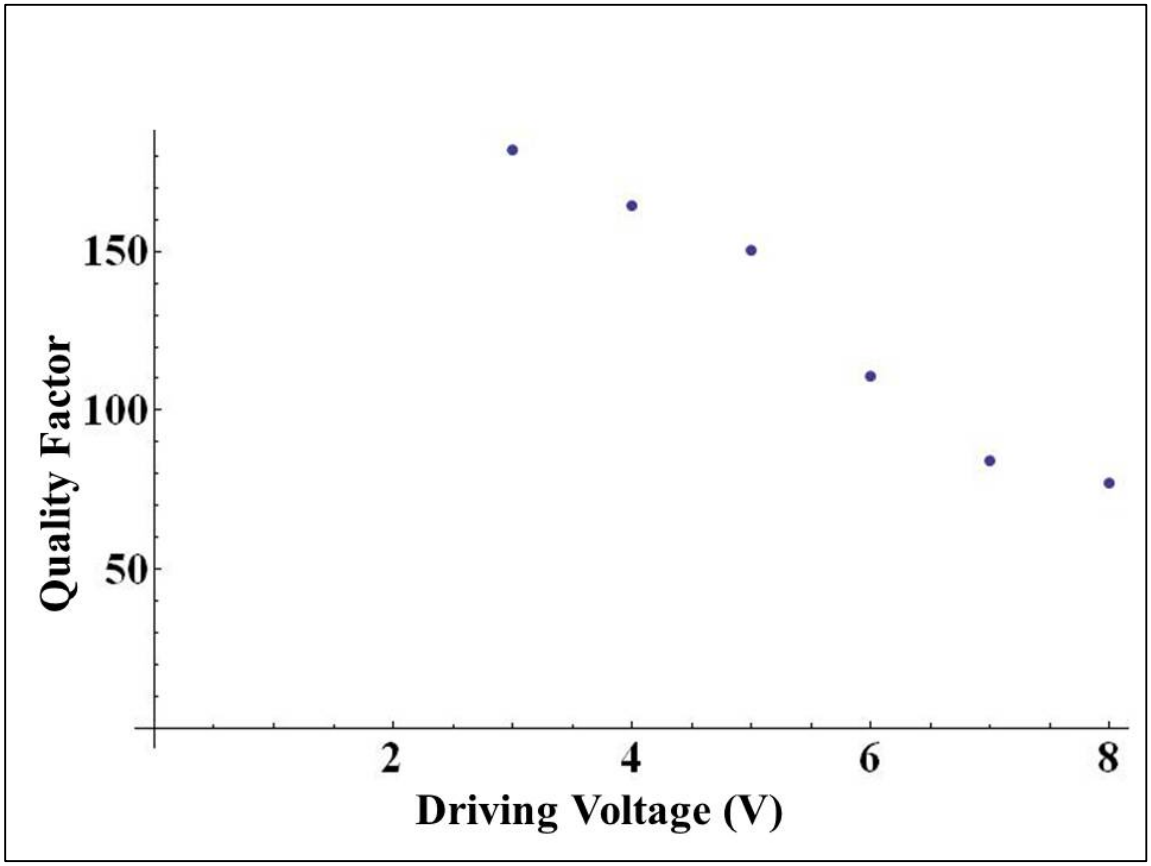


Figure 5.4: The quality factor of the observed resonance, driven at $\omega$. As the driving voltage increases, the quality factor can be seen to decrease irregularly.

# APPENDICES

# Appendix A

## Polar Representation of Resonance Peaks and Associated Calculations

### A.1 Polar representation

From Chapter 2, the equations describing the amplitude, *A*, and phase, $\varphi$, of a SHO (Eq. 2.6) being driven at frequency, $\omega$, are

$$A(\omega) = \frac{{}^{F_0}/_{m}}{\sqrt{\left(\omega_0^2 - \omega^2\right)^2 + (2\gamma\omega)^2}} \tag{2.9}$$

$$\tan\varphi(\omega) = \frac{2\gamma\omega}{\omega_0^2 - \omega^2} \tag{2.10}$$

where $\omega_0$ is the resonant frequency, and $\gamma$ is the damping factor. Using trig identities, we can solve for *A* in terms of $\varphi$:

$$\sin\varphi(\omega) = \frac{2\gamma\omega}{\sqrt{\left(\omega_0^2 - \omega^2\right)^2 + (2\gamma\omega)^2}} \tag{A.1}$$

$$A(\omega) = \frac{F_0}{m}\frac{\sin\varphi(\omega)}{2\gamma\omega} \propto \frac{\sin\varphi(\omega)}{\omega} \propto \sin\varphi(\omega) \tag{A.2}$$

which, when plotted in a polar representation will produce a circle. The last proportionality assumes that $\omega_0$ is much larger than $\Delta\omega$, the width of the resonance. In addition, when measuring the time derivative of the amplitude (such as the current output in HDR), the signal should be exactly a circle:

$$I(\omega) = I_0 \cos \omega t + \delta = \frac{dQ}{dt} = \frac{d}{dt} A(\omega) \cos \omega t \tag{A.3}$$

$$I_0(\omega) \propto \omega\, A(\omega) \propto \sin \varphi(\omega) \tag{A.4}$$

By searching for this circular behavior, the observation of resonance peaks becomes much easier in the presence of background which may not be constant as a function of frequency. However, it is also important to note frequency dependence of *A* and $\varphi$, respectively. Performing background subtraction as described in chapter 4 allows the recovery of curves which can be fit to Eq. 2.2.4 and 2.2.5.

In addition, as discussed in chapter 2, the resonant features involved in the harmonic detection of resonance, especially at higher harmonics, are more complicated than those of a SHO. Normally, however, they can be decoupled, in the polar representation, into circles, each of which is being traversed at an integer multiple of the frequency. The limaçon, for example, can be considered as 2 circles added together, with one moving through frequency space twice as fast as the other.

A.2 Quality Factor Determination

The quality factor, *Q*, of a resonator is defined by:

$$Q = {\omega_0}/{2\gamma} \tag{A.5}$$

where $\gamma$ is the damping factor as above. A typical method for determining *Q* for a resonator is the full width at half-maximum technique. In this approximation, the resonant frequency is divided by the width of the power spectrum of the oscillator (proportional to $A^2$). The width is defined by points on either side of the peak at half the amplitude of the maximum frequency (~$\omega_0$). This is effective since:

$$A^2(\omega_0) = \frac{1}{4\gamma^2\omega_0^2} \tag{A.6}$$

$$A^2\big(\omega_0(1 \pm \gamma)\big) \approx \frac{1}{8\gamma^2\omega_0^2} \tag{A.7}$$

ignoring terms in the denominator of order higher than $\gamma^3$. So the full width at half maximum will be $2\gamma$ and the method will give a close approximation of *Q* for sufficiently small damping.

In order to perform this calculation in the polar representation (useful the in the case of super-critical Duffing behavior), we realize that the half-maximum points of the power spectrum will be $1/\sqrt{2}$ of the maximum amplitude in the observed spectrum. This leads to a straight-forward bisection of the circle to determine the full width (see Fig. A.1). Even if points on the circle are not observed (for example if they fall in the unstable region of a Duffing-type peak), by approximating their position in the polar representation, a frequency can be determined.

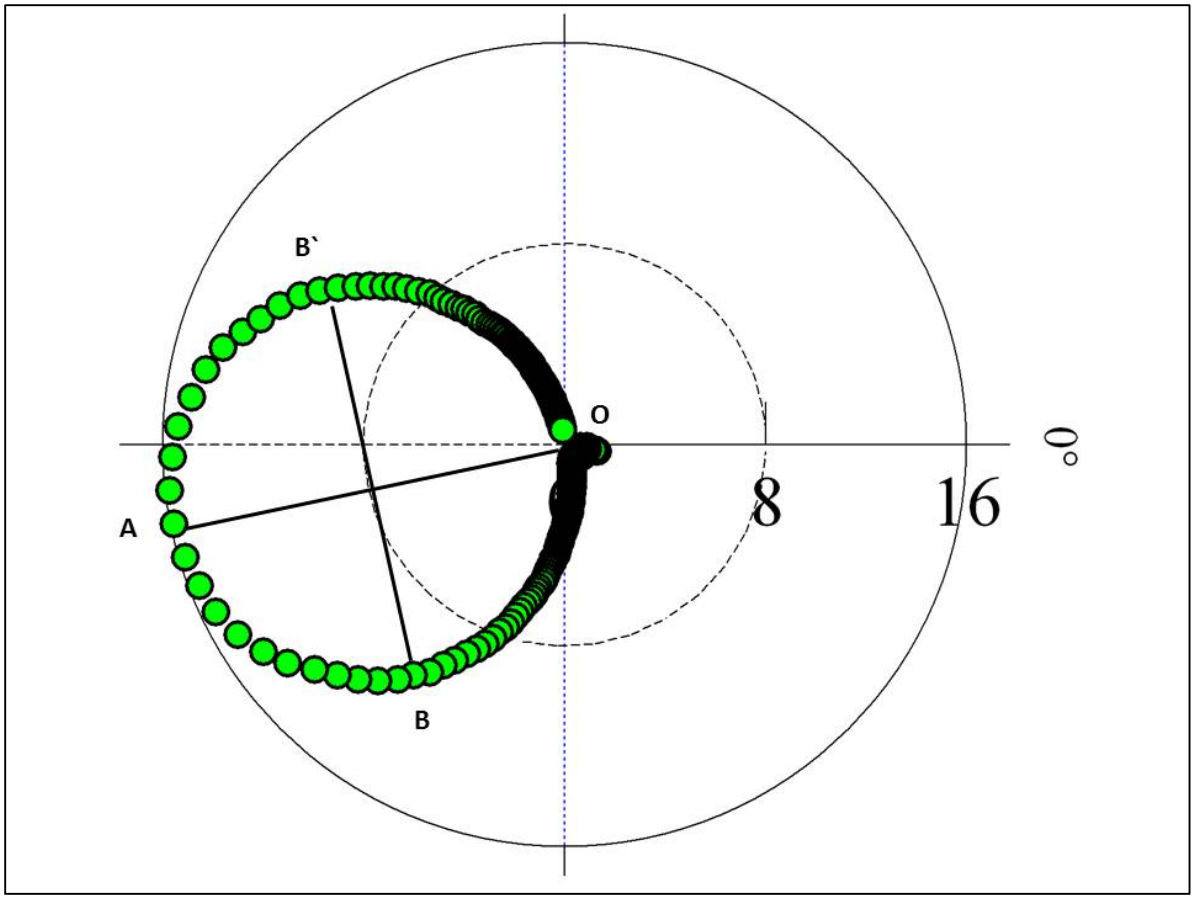


Figure A.1: Typical circular resonance behavior in ($A$, $\varphi$) polar coordinates. The point labeled O is off resonance and A is at the resonance peak. Points B and B` are used to determine the FWHM of the peak.

# Appendix B

## Configuration of HDR Setup for Use in an SEM

The electrical schematic can be seen in Figure 4.2. A Stanford Research Systems function generator (DS345 Synthesized Function Generator) was used to generate the driving signal and as a reference for the Lock-In Amplifier. The driving signal was biased by a custom built dc offset box powered by a 9V battery and tunable through the use of a potentiometer. BNC vacuum feedthroughs allowed the signal to be sent through the wall of the SEM (Hitachi SU6600) (Fig. B.1) and onto the custom built jig (Fig. B.2). Coaxial cable was used wherever the geometry of the setup permitted it to shield the signal.

The electrical signal produced by actuation of the cantilever was then sent to an FET (2N4416) mounted on the jig to reduce pickup and noise. The FET was remotely connected to a charge sensitive preamplifier (Amptek A250) raising the electrical signal to levels which could be observed by a Lock-In Amplifier (SRS SR844). Both the function generator and the Lock-In Amplifier were connected to a PC and controlled using a custom written LabView program which incremented the driving frequency and collected amplitude and phase data from the Lock-In. The external electrical setup can be seen in Figure B.3.

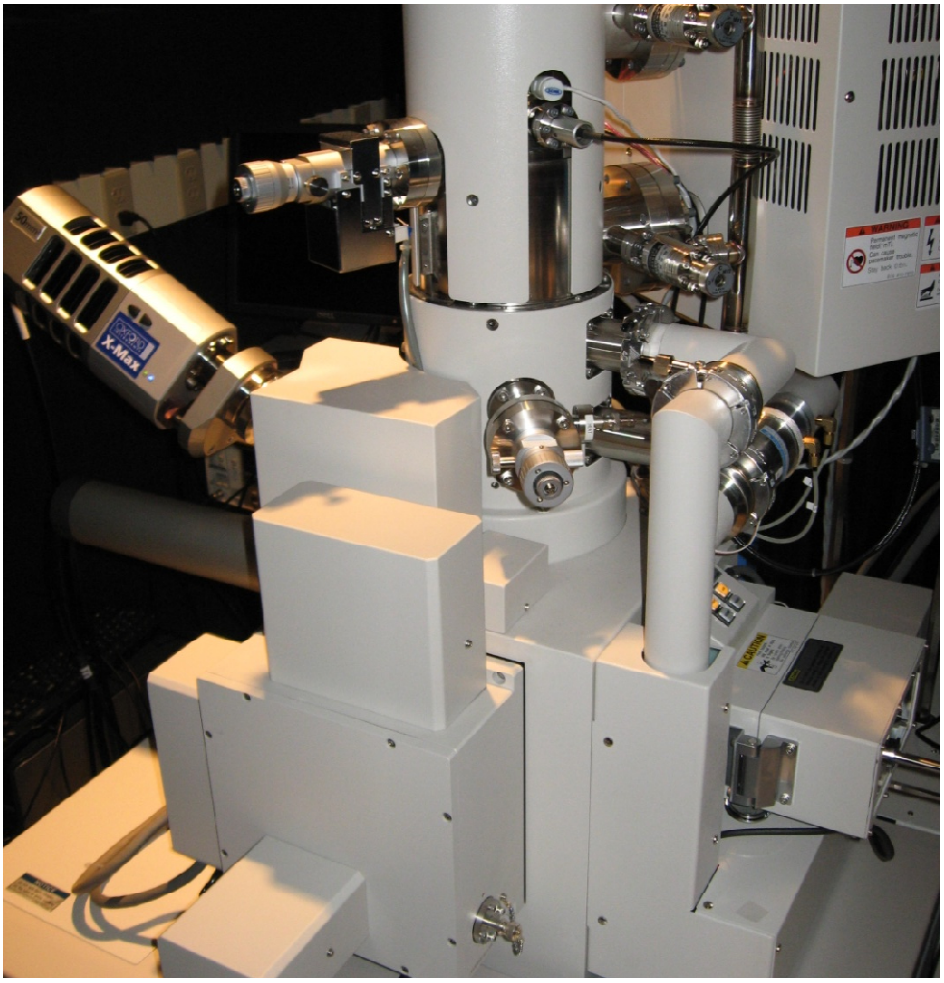

Figure B.1: SU6600 Scanning Electron Microscope

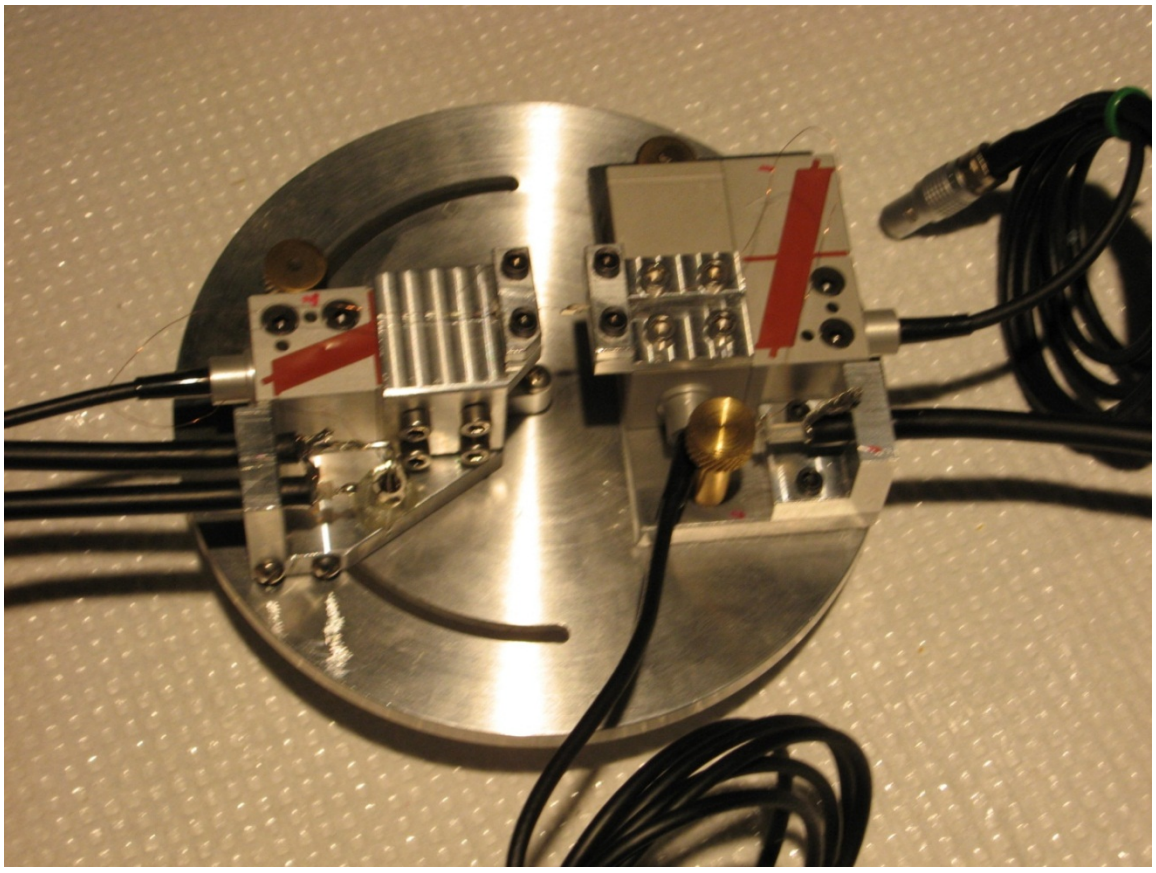

Figure B.2: Custom-built jig for manipulation of CCE setup. Three separate piezoelectric motors can be used to control the fine relative position of the cantilever and counterelectrode in each of the three spatial dimensions. Coarse positioning is achieved with the large gold colored screws, which move on tracks to change two spatial dimensions and 1 angular degree of freedom. The FET can be seen on the left hand mount, connected remotely to the preamplifier (not pictured).

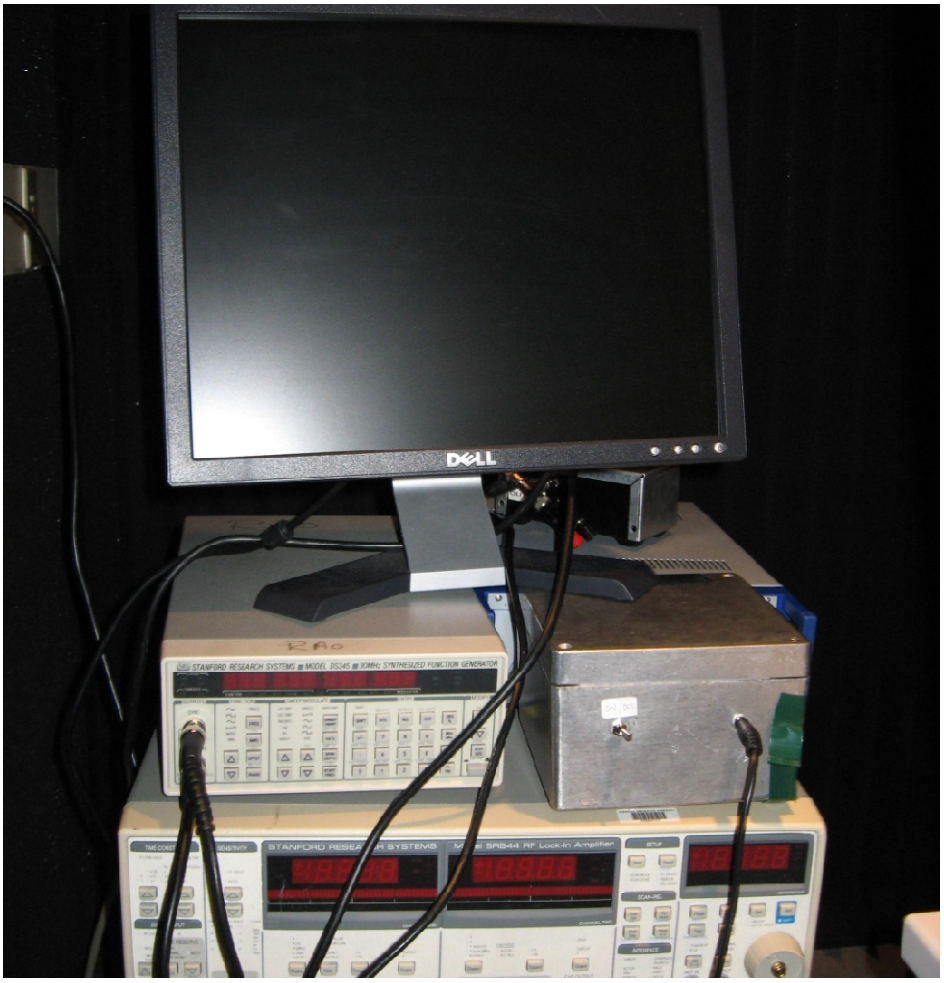


Figure B-3: External electrical setup for HDR experiments under vacuum. From top: monitor for use with controlling PC (not pictured) and dc bias unit, function generator and preamplifier power supply, lock-in amplifier.

## Appendix C

## Equipment List

1. Stanford Research Systems SR844 Lock-in Amplifier
2. Stanford Research Systems SR850 Lock-in Amplifier
3. Stanford Research Systems DS345 Synthesized Function Generator
4. Amptek A250 Charge Sensitive Preamplifier

REFERENCES

[1] S. Iijima, *Nature* 354, 56 (1991).

[2] S. Iijima and T. Ichihashi, *Nature* 363, 603 (1993).

[3] Z. W. Pan, Z. R. Dai, and Z. L. Wang, *Science* 291, 1947 (2001).

[4] D. N. McIlroy, D. Zhang, Y. Kranov, and M. Grant Norton, *Appl. Phys. Lett.* 79, 1400079 (2001).

[5] X. B. Zhang *et al., Europhys. Lett.* 27, 141 (1994).

[6] A B. Dalton, S. Collins, E. Muñoz, J. M. Razal, V. H. Ebron, J. P. Ferraris, J. N. Coleman, B G. Kim, and R. H. Baughman, *Nature* 423, 703 (2003).

[7] X. Wang, J. Song, J. Liu and Z. L. Wang, *Science* 316, 102 (2007).

[8] J. C. Johnson, H. Yan, R. D. Schaller, L. H. Haber, R. J. Saykally, and P. Yang, *J. Phys. Chem. B* 105, 11387 (2001).

[9] H. Liu, J. Kameoka, D. A. Czaplewski, and H. G. Craighead, *Nano Lett.* 4, 671 (2004).

[10] C. Stampfer, T. Helbling, D. Obergfell, B. Schöberle, M. K. Tripp, A. Jungen, S. Roth, V. M. Bright, and C. Hierold, *Nano Lett.* 6, 233 (2006).

[11] X. Wang, X. Wang, J. Zhou, J. Song, J. Liu, N. Xu, and Z. L. Wang, *Nano Lett.* 6, 2768 (2006).

[12] P. R. Bandaru, C. Daraio, S. Jin and A. M. Rao, *Nature Materials* 4, 664 (2005).

[13] K. Jensen, J. Weldon, H. Garcia, and A. Zettl, *Nano Lett.* 7, 3508 (2007).

[14] P. Poncharal, Z. L. Wang, D. Ugarte, and W. A. de Heer1, *Science* 283, 1513 (1999).

[15] C. Nam, P. Jaroenapibal, D. Tham, D. E. Luzzi, S. Evoy, and J. E. Fischer, *Nano Lett.* 6, 153 (2006).

[16] X. D. Bai, P. X. Gao, Z. L. Wang, and E. G. Wang, *Appl. Phys. Lett.* 82, 4806 (2003).

[17] X. L. Feng, C. J. White, A. Hajimiri, and M. L. Roukes, *Nature Nanotech.* 3, 342 (2008).

[18] G. Abadal, Z.J. Davis, B. Helbo, X. Borrise, R. Ruiz, A. Boisen, F. Campabadal, J. Esteve, E. Figueras, F. Perez- Murano, and N. Barniol, *Nanotechnology* 12, 100 (2001).

[19] J. Verd, G. Abadal, J. Teva, M. Gaudo, A. Uranga, X. Borrise, F. Campabadal, J. Esteve, E. Costa, F. Murano, Z. Davis, E. Forsen, A. Boisen, and N. Barniol, *J. Micro. Sys.* 14, 508 (2005).

[20] K. Ekinci and M. Roukes, *Rev. Sci. Instrum*. 76, 061101 (2005).

[21] C. Ke, H. D. Espinosa, *J. Appl. Mech.* 72, 721 (2005).

[22] D. Dickel, M. J. Skove, and A. M. Rao, *J. Appl. Phys.* 106, 044515 (2009).

[23] J. Gaillard, M. J. Skove, R. Ciocan, and A. M. Rao, *Rev. Sci. Instr.* 88, 243113 (2006).

[24] G. Keskar, B. Elliott, M. J. Skove, and A. M. Rao, *IEEE Sensors J.* 8, 1848 (2008).

[25] J. D. Lawrence, *A Catalog of Special Plane Curves* Dover, New York, 1972, p. 113.

[26] B. Elliott, H. Behlow, D. Dickel, G. Keskar, M. J. Skove, A. M. Rao, *Rev. Sci. Instr.* 82, 055103 (2011).

[27] F. R. Blom, S. Bouwstra, M. Elwenspoek, and J. H. J. Fluitman, *J. Vac. Sci. Tech. B* 10, 19 (1992).

[28] G. Keskar, B. Elliott, J. Gaillard, M. J. Skove, and A. M. Rao, *Sens. & Actuators A* 147, 203 (2008).

[29] S. Bianco *et al., J. Vac. Sci. Tech B* 24, 1803 (2006).

[30] S. Kim, K. D. Kihm, and T. Thundat, *Exp. Fluids* 48, 721 (2010).

[31] D. N. McIlroy, D. Zhang, Y. Kranov, and M. G. Norton, *Appl. Phys. Lett.* 79, 1540 (2001).

[32] D. N. McIlroy, A. Alkhateeb, D. Zhang, D. E. Aston, A. C. Marcy, and M G. Norton, *J. Phys: Condensed Matter* 16, 415 (2004).

[33] K. Sanada, Y. Takada, S. Yamamoto, and Y. Shindo, *J. Solid Mech. And Mat. Eng.* 2, 1517 (2008).

[34] S. Hokushin, L. Pan, Y. Konishi, H. Tanaka, and Y. Nakayama, *Jpn. J. Appl. Phys.* 46, 565 (2007).

[35] K.W. Park, Y. E. Sung, S. Han, Y. Yun, and T. Hyeon, *J. Phys. Chem. B*, 108 939 (2004).

[36] L. Pan, M. Zhang, and Y. Nakayama, *J. Appl. Phys.* 91, 10058 (2002).

[37] P. R. Bandaru, C. Daraio, K. Yang, and A. M. Rao, *J. Appl. Phys.* 101, 094307 (2007).

[38] L. Pan, T. Hayashida, A. Harada, and Y. Nakayama, *Physica B: Cond. Matter* 323, 350 (2002).

[39] T. Hayashida, L. Pan, Y. Nakayama, *Physica B: Cond. Matter* 323, 352 (2002).

[40] X. Chen, S. Zhang, D. A. Dikin, W. Ding, R. S. Ruoff, L. Pan and Y. Nakayama, *Nano Letters* 3, 1299 (2003).

[41] Q. Zhang, J. Qi, X. Lia, and Y. Zhang, *Nanoscale* 3, 3060 (2011).

[42] J. Lee and D. J. Thompson, *J. Sound and Vibration* 239, 297 (2000).

[43] A. F. da Fonseca and D. S. Galvao, *Phys. Rev. Lett.* 92, 175502 (2004).

[44] G. Zhang and Y. Zhao, *J. Appl. Phys.* 95, 267 (2004).

[45] C. Y. Lee, H. C. Zhuo, and C. W. Hsu, *J. Sound and Vibration* 324, 179 (2009).

[46] Z. J. Davis *et al., Sens. & Actuators A* 105, 311 (2003).

[47] D. A. Dikin, X. Chen, W. Ding, G. Wagner, and R. S. Ruoff, *J. Appl. Phys.* 93, 226 (2003).

[48] R. Ciocan, J. Gaillard, M. J. Skove, and A. M. Rao, *Nano Letters* 5, 2389 (2005).

[49] S. Sato, L. Pan, Y. Nakayama, and S. Akita, *Microprocesses and Nanotechnology*, 468 (2007).

[50] S. Perisanu, T. Barois, A. Ayari, P. Poncharal, M. Choueib, S. T. Purcell, and P. Vincent, *Phys. Rev. B* 81, 165440 (2010).

[51] Y. Lin, B. Zhou, K. A. Shiral Fernando, P. Liu, L. F. Allard, and Y. P. Sun, *Macromolecules* 36, 7199 (2003).

[52] Rowan Blake, Y. K. Gun'ko, J. Coleman, M. Cadek, A. Fonseca, J. B. Nagy, and W. J. Blau, *J. Am. Chem. Soc.* 126, 10226 (2004).

[53] Y. Lin, A. M. Rao, B. Sadanadan, E. A. Kenik, and Y. P. Sun, *J. Phys. Chem. B* 106, 1294 (2002).

[54] C. Zhao, L. Ji, H. Liu, G. Hu, S. Zhang, M. Yang, and Z. Yang, *J. Solid State Chem.* 177, 4394 (2004).

[55] L. Lacerda *et al.*, *Advanced Materials* 20, 225 (2008).

[56] L. Lacerda *et al.*, *Nanomedicine* 3, 149 (2008).

[57] E. Mooney, P. Dockery, U. Greiser, M. Murphy, and V. Barron, *Nano Lett.* 8, 2137 (2008).

[58] X. Lepró, M. D. Lima, and R. H. Baughman, *Carbon* 48, 3621 (2010).

[59] H. Dai, E. W. Wong, and C. M. Lieber, *Science* 272, 523 (1996).

[60] T. W. Ebbesen, H. J. Lezec, H. Hiura, J. W. Bennett, H. F. Ghaemi, and T. Thio, *Nature* 382, 54 (1996).

[61] M. M. J. Treacy, T. W. Ebbesen, and J. M. Gibson, *Nature*, 381, 678 (1996).

[62] J. P. Lu, *Phys. Rev. Lett.* 79, 1297 (1997).

[63] E. W. Wong, P. E. Sheehan, and C. M. Lieber, *Science* 277, 1971 (1997).

[64] A. Kis, K. Jensen, S. Aloni, W. Mickelson, and A. Zettl, *Phys. Rev. Lett.* 97, 025501 (2006).

[65] P. Zhang, P. E. Lammert, and V. H. Crespi, *Phys. Rev. Lett.* 81, 5346 (1998).

[66] A. Eichler, J. Moser, J. Chaste, M. Zdrojek, I. Wilson-Rae, and A. Bachtold, *Nature Nanotech.* 6, 339 (2011).